Rescuing early Parkinson-induced hyposmia prevents dopaminergic system failure

Ulrike Pech[1,2, †], Jasper Janssens[1,3, †], Nils Schoovaerts[1,2], Samira Makhzami[1,3], Gert Hulselmans[1,3], Suresh Poovathingal[1,3], Carles Calatayud Aristoy[1,2], Adekunle T. Bademosi[1,2], Jef Swerts[1,2], Ann Geens[1,2], Sven Vilain[1,2, ‡], Stein Aerts[1,3] and Patrik Verstreken[1,2,*]

[1] VIB-KU Leuven Center for Brain & Disease Research
[2] KU Leuven, Department of Neurosciences, Leuven Brain Institute
[3] KU Leuven, Department of Human Genetics, Leuven Brain Institute
3000 Leuven, Belgium

[*] corresponding author: patrik.verstreken@kuleuven.be
[†] These authors contributed equally to this work
[‡] Present address: Istanbul Medipol University, Istanbul, Turkey

Summary

The diagnosis of Parkinsonism is based on motor symptoms that are caused by reduced dopaminergic output. However, decades earlier, patients report non-motoric problems, including hyposmia. It is not known if non-motor and motor defects are causally connected. Using unbiased methods, we identified common synaptic defects in cholinergic neurons across premotor-stage familial fly Parkinson models and in patient samples. These early synaptic defects cause olfactory performance problems. Correcting these defects specifically in olfactory cholinergic interneurons in flies or inducing cholinergic signaling onto Parkinson mutant human induced dopaminergic neurons *in vitro* using nicotine, both rescue age-dependent dopaminergic neuron decline. Our approach reveals shared pathways of synaptic failure in cholinergic neurons that drive dopaminergic dysfunction across familial Parkinson models.

Introduction

Parkinson's disease (PD) is a complex multifactorial neurodegenerative disease that affects millions. Dopaminergic neuron (DAN) death in the *Substantia nigra* causes motor defects in patients. However, 97% of patients suffer from non-motoric dysfunction decades earlier, including constipation, REM sleep disorder and hyposmia [1-5]. These non-motor defects in PD are often overlooked because they occur before disease diagnosis and thus, they do not belong to the normal clinical work up. Furthermore, non-motoric defects are largely non-responsive to dopamine replacement therapy suggesting other cell types are involved [6]. It is not known if the cells and mechanisms that underlie these early symptoms drive the harm in other brain areas at later stages, including DAN system failure.

Hyposmia, the reduced ability to discern odors, is one of the earliest defects associated with familial and sporadic Parkinsonism [3; 5; 7; 8]. These patients show difficulties to classify odors: they often perceive banana odor as motor oil or beer odor as fruit in standardized odor identification tests (UPSIT) [9]. These observations suggest that hyposmia in Parkinsonim is caused by a defect in higher order perception, consistent with the observations that first order olfactory receptor cells of the nasal epithelium are not majorly affected in patients [10; 11]. The synaptic site of second-order olfactory neurons, the olfactory bulb, is modulated by basal forebrain cholinergic neurons and local GABAergic and dopaminergic interneurons [12]. While these DAN do not degenerate in Parkinsonism, it has been suggested there is local impairment of cholinergic transmission in the olfactory bulb of Parkinson's disease patients and vertebrate models [13-15], but the molecular defects are elusive.

There are only few models to study hyposmia in Parkinsonism and most are based on the use of toxins or expression of mutant alpha-synuclein [16]. While this may recapitulate aspects of the disease, they bias the disease mechanisms to known phenomena associated with the specific

model. Modelling approaches to PD are further hindered due to the large number of mutated genes. These mutations affect various biological functions and therefore it is currently hard to unveil the specific pathways and cell types that are at the basis of the early defects in the disease. So far, mutations in more than 20 genes have been identified that cause familial forms of Parkinsonism [17]. These genes cause defects in a diverse range of processes including mitochondrial function, endocytosis, lysosomal function, autophagy and protein translation [6]. Nonetheless, these mutations do result in overlapping motor and non-motor defects, including hyposmia. This raises the question of whether defective mechanisms across the genetic space of PD converge on a common biological process and affect similar cell types beyond DAN.

In this study, we utilized a variety of *Drosophila* models, brain samples from postmortem patients, and mutant induced human neurons to investigate cellular dysfunction preceding the diagnosis of motor defects in Parkinsonism. Our research identified common cell types and processes affected across mutants, including synaptic problems in cholinergic interneurons that result in hyposmia. This is significant because we show that a decrease in cholinergic signaling leads to failure of the DAN system later in life, both in flies and in mutant induced human neurons. Our research emphasizes the significance of early diagnosis and treatment of non-motor symptoms in Parkinsonism.

Results

A new collection of familial PD knock-in models.

The identification of non-DAN cell types that are affected by PD is hindered because mutations in over 20 genes have been linked to familial forms of the disease [17]. We therefore created a new, isogenic collection of *Drosophila* PD models, representing the variety of affected pathways and clinical manifestations in this disease [6]. We replaced the *Drosophila lrrk, Chchd2, rab39, auxilin*

(aux), *synaptojanin (synj)* and *Pink1* genes by either wild type and pathogenic mutant human or *Drosophila* CDS and verified that the wildtype and pathogenic mutant human CDS (*LRRK2*, *CHCHD2*, *RAB39B* and *PINK1*) or *Drosophila* CDS (*DNAJC6 (Aux)* and *Synj1*) were expressed at endogenous levels (Figure 1A, Figure S1A). While wildtype knock-ins were similar to controls, the PD models showed defects akin to those seen in previously described mutants, including reduced lifespan under starvation, mitochondrial membrane potential- and electrophysiological defects and age-dependent decline in DAN-mediated motor climbing ability [18-27] (Figure 1B, Figure S1B-D). Hence, we established a well-controlled collection of PD models.

Cholinergic olfactory projection neurons are impaired across PD fly models at premotor stage.

We used unbiased single cell RNA sequencing of entire brains of young (5-day old) animals to define cell types affected by pathogenic PD mutations at early, premotor stages. We pooled 108k newly sequenced cells from six of these mutants with the 118k wildtype cells from our original atlas leading to 186 clusters, of which 81 were annotated to known cell types[28; 29] (Figure 2A,B, Figure S1E). PD mutant cells equally mixed with the cells of the original fly brain cell atlas and the frequency of recovered cell types were similar between control and mutant brains (including DAN; Figure 2C-H, Figure S2A and B). We further did not find any cell type that showed higher or lower expression of the knocked-in CDS (Figure S2C). Thus, cellular identity and cellular composition are preserved in young PD fly models.

For every cluster, we then compared gene expression between cells from mutants and controls using two independent algorithms (wilcoxon and deseq2, [30]), and find both methods correlated

well (average Spearman correlation of signed p-value > 0.8 to > 0.95). However, the number of differentially expressed genes (DEG) is largely dependent on the number of cells present in a cluster. To correct for this bias, we fitted a negative binomial model that correlated the number of DEGs and cell cluster size in each mutant (Figure S2D and E). Using the residuals of this model we found eight predominantly affected cell types across the mutants. We also found cell types uniquely affected in some mutants, e.g., glial subtypes that were affected in *PINK1*^{P399L}. The commonly affected cell types included cholinergic olfactory interneurons (Olfactory projection neurons - OPN and Kenyon cells), cholinergic interneurons of the visual system, and other to-be-identified cell types (Figure 2B-H, black cells). Hence, independent of the genetic origin of disease, some cell types were commonly affected across our young familial PD models.

OPN are higher order projection neurons that control innate olfactory processing and odor classification [31]. Hyposmia is also one of the earliest defects associated with familial and sporadic Parkinsonism [5; 8] with patients having difficulties to classify odors in standardized UPSIT tests [9-11]. We determined if our young PD models also showed olfactory performance defects and if these originated from OPN dysfunction. Control and wild type knock-in flies showed robust odor preference in two separate tests, while the pathogenic mutant CDS knock-in flies were indecisive (except for CHCHD2^{R145Q}; Figure 2I, Figure S3). We then expressed the wild type CDS of each of the genes *selectively* in the OPN of the pathogenic knock-in mutant flies (e.g. GH146-Gal4>UAS-Rab39 in *Rab39B*^{G192R}). This restored olfactory performance (Figure 2J, Figure S3). In contrast, expressing wild type CDS in T1-interneurons of the visual system in *Rab39B*^{G192R} did not improve their olfactory behavior (Figure 2J, Figure S3). Hence, the odor choice performance defect of these PD models is caused by loss-of-gene-function in OPN. Interestingly, expression of human LRRK2 in OPN rescued the *lrrk* null mutant olfactory

preference defect, but not the defect in LRRK2^{G2019S}, agreeing with this being a dominant gain-of-function mutant [32].

Common synaptic genes and pathways are deregulated in cholinergic brain regions of fly PD models and human PD patients.

To identify the nature of the OPN dysfunction we listed the deregulated genes for each mutant in the commonly affected cell types. There were mutation-unique DEG in each PD mutant, but also a significant overlap in DEGs between the models (Figure 3A). To determine if aspects of these findings translate in PD patient brains, we conducted single cell RNAseq on cholinergic brain region samples (*nucleus basalis of Meynert*, NBM, *nucleus accumbens*, Nac, *putamen*, Put) from five brains of *LRRK2* mutant patients and five brains from unaffected individuals and identified the DEG (Figure S4A and B). The fraction of cholinergic neurons was too small to be analyzed separately in any sample (Figure S4C), so we pooled all neuronal cell types within a sample for analysis and found a remarkable overlap of DEG in these three brain regions of PD patients and DEG common to our fly PD models (Figure 3B). In the *nucleus basalis*, for example, 20% of the DEG that have an ortholog gene in the fly were also found among the most deregulated genes across PD fly models. The *nucleus basalis* contains the largest collection of cholinergic projection neuron cell bodies in the brain and defects in this area have been associated with PD [33]. Of the three regions we have analyzed, the *nucleus basalis* contained the highest fraction of cholinergic neurons, hence this region was used for further analyses (Figure S4C). We analysed DEG using Gorilla gene ontology enrichment [34] and found that the processes that were most strikingly enriched in both fly models and human NBM were those related to synaptic function (Figure 3C). Indeed, half of the DEGs found in human and flies are present in the synapse-specific portal SynGo [35] (Figure 3D). We found enrichment for presynaptic function, including

synaptic exocytosis, axon guidance, synapse organization, ion transport and protein homeostasis. We also found enrichment of RNA regulation and mitochondrial function that are also important for the functioning of synaptic terminals [19; 36-38]. Thus, cholinergic neurons of fly PD models and human PD patients both showed preferential transcriptional deregulation of synaptic genes (Figure 3C, D, Figure 4).

Impairment of OPN synapses in PD models is rescued by synaptic autophagy.

The transcriptional deregulation predicts synaptic alterations in affected cell types. We therefore expressed the Ca^{2+}-sensor GCaMP3 in OPN and monitored synaptic terminal function through a small window in the head capsule of living flies. Stimulation only caused weak Ca^{2+}-responses in the five hyposmic PD mutants (Figure 5A-D). In contrast, wild type CDS knock-in animals, or PD mutants expressing wild type CDS *selectively* in their OPN showed robust synaptic Ca^{2+} signals (Figure 5D). We also quantified synaptic morphology by determining the synaptic area marked by GFP (live and fixed) and found that the synaptic area was larger in the pathogenic mutants compared to controls despite similar GFP expression levels (Figure 5E). Again, all these defects were rescued by OPN-selective expression of the wild type CDS, but $LRRK2^{G2019S}$ behaved, expectedly, as a dominant mutant (Figure 5E). Thus, OPN of young PD mutants displayed cell-autonomous presynaptic defects.

To define which of the synaptic processes identified by the DEG was critical to cause OPN dysfunction and hyposmia, we up- or downregulated selected genes in OPN of our PD models and asked if this restored the olfactory preference defect. Only the upregulation of protein homeostasis/autophagy genes, including *atg8*, *lamp1* and *hsc70*, rescued the defect across PD models (Figure S5). We independently confirmed this by using OPN-specific expression of

endoA^{S75D}. EndoA is a synapse-specific protein [39; 40] and a mutation in the human *EndoA* gene, *SH3GL2*, as well as two independent GWAS signals in the vicinity confer risk to PD [41-43]. We showed previously that the phosphomimetic mutation S75D in EndoA drives macroautophagy specifically at presynaptic terminals [44]. Expression of *endoA*^{S75D} , hence induction of synpaptic autophagy, in OPN of the PD mutants also rescued the olfactory performance defect (Figure 5F), the synaptic dysfunction (Ca^{2+} response to stimulation) (Figure 5G) and defects in synaptic morphology (synapse area marked by GFP) (Figure 5H). This suggested that impaired protein homeostasis at OPN synapses caused hyposmia across our PD models.

Age-dependent dopaminergic decline in PD model flies.

DAN dysfunction is notorious in PD, but DAN were not among the most affected cell types in young PD fly models. We thus asked whether DAN might become affected during aging and conducted single-cell-RNA-sequencing of brains of aged LRRK2 mutants. This identified increased transcriptomic changes across the brain and now included the protocerebral anterior medial neuron cluster (PAM) DAN as an affected celltype (Figure 6A). These findings were consistent with the negative geotaxis climbing defect (Startle-induced negative geotaxis (SING)) we saw in aged PD mutant flies (Figure 1B); indeed, SING depends on functional PAM neurons [27]. Importantly, transcriptomic alterations in aged LRRK2 mutants are different from those in aged controls (Figure 6B).

To assess DAN function directly, we expressed GCaMP3 *selectively* in PAM DAN using R58E02-Gal4 and imaged stimulation-induced Ca^{2+}-transients in synaptic terminals (Figure 6C). While 5-day old flies were similar to controls, the amplitude of the Ca^{2+}-transients progressively declined in older PD mutants (except Rab39B^{G192R}) (Figure 6D). We further quantified the

synaptic area of DAN in the mushroom body lobes using immunohistochemistry (Figure 6E) and find the synaptic area gradually declining in ageing PD mutants (Figure 6F,G). Hence, while in young PD mutants PAM DAN are not affected, there is progressive deterioration of PAM DAN in PD models upon ageing.

Restoring OPN function or cholinergic signaling prevents age-dependent decline of DAN function across PD models.

To test if the non-motor cholinergic defect in young animals causally links to DAN dysfunction in old animals, we selectively rescued the OPN and quantified DAN-related phenotypes in the aging PD models. We started by conducting single-cell RNA seq on aged LRRK2^{G2019S} mutants that express *endoA*^{S75D} selectively in OPN from young age onwards (we expressed GCAMP3 as a control). We then compared DEG in every cell type of the brain to wildtype aged controls and found that LRRK^{G2019S} animals expressing endoA^{S75D} in OPN not only had a reduced number of DEG in OPN, but also in several other cell types across the brain, including DAN (Figure 7A). To assess this effect further we expanded our analysis to other PD mutants. We expressed the wild type CDS or *endoA*^{S75D} selectively in OPN and quantified DAN-related phenotypes in the aging PD models. The decline in DAN synaptic area was significantly rescued by either manipulation across PD models (Figure 7B). Likewise, we found a significant improvement of SING (Figure 7C). To further determine if this rescue was caused by cholinergic transmission, we food-supplemented PD mutants with nicotine, a nicotinergic acetylcholinergic receptor (nAchR) agonist, from day 1 post eclosion onwards. While this did not improve OPN function itself (Figure 8A), it was effective at rescuing the PAM DAN defects: We recorded significantly improved SING, synaptic Ca^{2+}-transients and synaptic morphology in nicotine-fed LRRK2^{G2019S} mutants at 15 -days of age compared to non-fed mutants (Figure 8B). Hence, restoring or

replacing cholinergic OPN output was sufficient to rescue progressive DAN dysfunction in PD models.

We next knocked-in the LRRK2G2019S mutation in the standard human KOLF2.1J iPS cell line [45] and differentiated these into ventral midbrain DAN (Figure 8C, Figure S6A-E). The neurons were further transfected with GCaMP6. For a fraction of neurons, the medium was supplemented with nicotine for 20 days. Nicotine was then removed from the medium and Ca^{2+} activity recorded 2 days later. While spontaneous Ca^{2+} activity and transient amplitude in 62-day-old *LRRK2*^{G2019S} DAN not supplemented with nicotine were significantly lower compared to isogenic controls (Figure 8D), *LRRK2*^{G2019S} DAN supplemented with nicotine were statistically indistinguishable from isogenic controls (with or without nicotine). This rescue was dependent on cholinergic signaling because addition of the nAchR blocker mecamylamine to the nicotine treatment abolished this rescue (Figure 8D). These results indicate that cholinergic signaling prevents dopaminergic decline in fly and human PD models.

Discussion

PD is currently diagnosed based on motor defects that only occur following significant DA degeneration. However, cholinergic defects are observed in patients in several brain regions, including the olfactory bulb [15; 33; 46] and the occipital cortex [47; 48]. Cholinergic problems also correlate with several non-motor symptoms, including impaired olfactory and visual processing [49]. We recapitulated key aspects of this in flies, showing the engagement of transmitter systems other than the dopaminergic system in early disease stages. Importantly, our data suggest these early cholinergic defects causally and cell-non autonomously relate to the DAN failure later in life. This is in line with epidemiological observations that suggest nicotine uptake through

chronic smoking is protective to PD [50; 51], and it is consistent with our finding that nicotine supplementation alleviates dysfunction of human induced PD-mutant DAN. While PD is currently diagnosed based on motor defects that occur following significant dopaminergic neuron degeneration, our work now suggests that the detection of specific cholinergic interneuron dysfunction, is a better prodromal signal of disease.

Our findings reveal a common trigger relevant for both familial and idiopathic cases. Observations of Lewy body pathology in postmortem samples suggest the disease may nucleate at specific sites and then propagate. This includes spreading of the disease between the gut and the brain as well as early aggregation of alpha-synuclein in the olfactory bulb [52]. The presence of protein aggregates in these areas is consistent with protein homeostasis defects that ultimately contribute to the aggregation of alpha-synuclein [53-56]. In idiopathic disease, there is some evidence this is because the gut and olfactory bulb are more easily exposed to environmental toxins that cause protein misfolding and aggregation [46]. Fly olfactory projection neurons, like human basal forebrain cholinergic neurons and striatal cholinergic interneurons, are characterized by large neuronal arbors and high activity [57-59]. Such neurons are thought to be particularly vulnerable to alterations in protein homeostasis [60; 61] and our work now indicates that the defects induced by different familial PD mutations converge on protein homeostasis defects, particularly in cholinergic interneurons. We propose a model where the earliest phase of both familial and idiopathic PD is characterized by either genetic or environmental insults that, through different mechanisms, cause protein homeostasis dysfunction in the olfactory cholinergic neurons and this ultimately triggers the spread of disease including DAN defects. This also implies that the defects in proteostasis are already at play at the earliest phases and, as we show here, tackling this defect is therapeutically important to protect DAN.

Acknowledgments: We thank Eren Can Eksi, Vinoy Vijayan, Liesbeth Deaulmerie, Willem van den Bergh, Marianna Decet and Sara Aibar, Bart De Strooper, Joris de Wit, Roman Prashberger, the members of the Verstreken and Aerts labs and the VIB BioImaging core for help and comments. We thank Atefeh Pooryasin and the Bloomington Drosophila Stock Center (NIH P40OD018537) for fly lines, and the Parkinson's UK Brain Bank at ICL for patient tissue. KOLF2-1J was a gift by William C. Skarnes from The Jackson Laboratories. Research support was provided by ERC CoGs (PV and SA), the Research Foundation Flanders (FWO), the Hercules Foundation, a Methusalem grant of the Flemish government, IMI2, Opening the Future and VIB. UP was supported by a fellowship from DFG; AB was supported by an EMBO long term fellowship and SV was supported by a fellowship from FWO. This research was also funded in part by Aligning Science Across Parkinson's (ASAP-000430) through the MJFF. PV is an alumnus of the FENS Kavli Network of Excellence.

Author contributions:

Conceptualization: UP, SV, PV

Methodology: UP, JJ, NS, SM, GH, SP, CCA, JS, SV

Investigation: UP, JJ, AB, AG

Visualization: UP, JJ, CCA, PV

Funding acquisition: PV, SA, UP, SV, AB

Project administration: PV

Supervision: SA, PV

Writing – original draft: UP, PV

Writing – review & editing: all

Competing interests: Authors declare that they have no competing interests.

Data and materials availability: Plasmids and fly lines generated in this study are available on request. Codes and data sets generated in this study will be stored online and available upon publication.

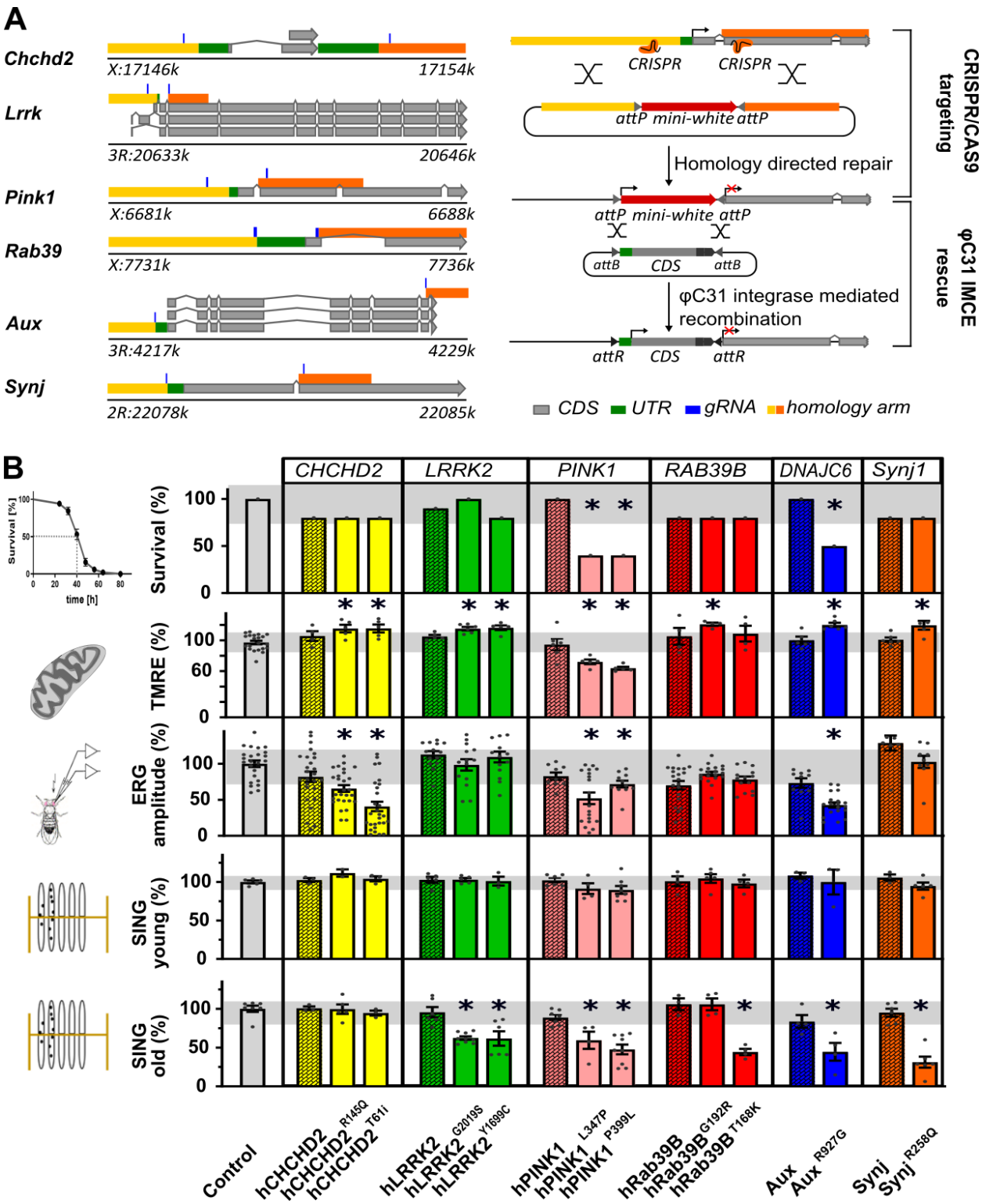

Figure 1. A new collection of familial PD knock-in models. See also Figure S1.

(A) Scheme of the knock-in strategy where the first common exon in all *Drosophila* transcripts (left) is first replaced by an attP-flanked mini-*white* gene using CRISPR/Cas9 mediated homologous recombination, creating a null mutant, and then replaced by wildtype or pathogenic

mutant human or fly CDS using PhiC31 mediated integration (right). The chromosomal positions of the targeted genes are indicated. All knock-ins were generated in the same isogenic genetic background (cantonized w^{1118}, see Methods).

(B) Phenotypes relevant to modeling Parkinson's disease in *Drosophila*: (1) Median survival under starvation. n>50 animals per genotype. (2) TMRE fluorescence intensity as a readout of mitochondrial membrane potential at individual neuromuscular junction (NMJ) synaptic boutons in 3rd instar larvae. n≥4 animals per genotype and 10 boutons from ≥3 NMJs per animal. (3) Depolarisation amplitude of electroretinograms (ERGs) recorded after 7 days of constant light exposure. n≥20 animals per genotype. (4) Quantification of startle-induced-negative geotaxis (SING) assayed 5±1 d after eclosion (young) and 25±1 d after eclosion (old). 95% of *pink1* mutants died < 25 d; they were tested at 15 d after eclosion. All values are shown normalized to the average of the wildype control (see methods) and the control variance is indicated by a grey zone in each assay. Bars represent mean ± s.e.m; *, $p<0.05$ in ANOVA followed by Dunnett's test.

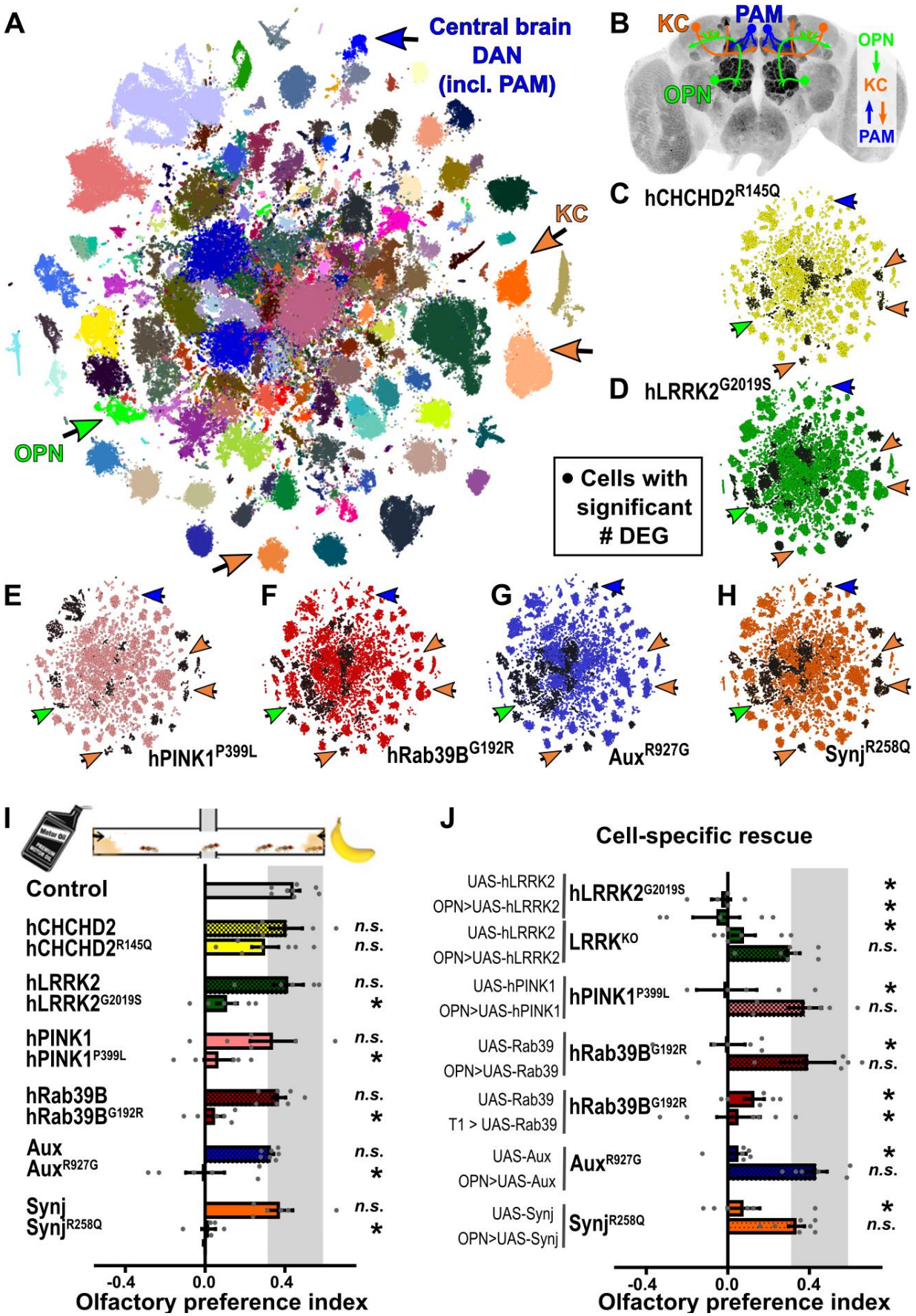
A
Central brain DAN (incl. PAM)
KC
OPN
B
KC
PAM
OPN
OPN
KC
PAM
C hCHCHD2R145Q
D hLRRK2G2019S
• Cells with significant # DEG
E
hPINK1P399L
F
hRab39BG192R
G
AuxR927G
H
SynjR258Q
I
Control
hCHCHD2
hCHCHD2R145Q
hLRRK2
hLRRK2G2019S
hPINK1
hPINK1P399L
hRab39B
hRab39BG192R
Aux
AuxR927G
Synj
SynjR258Q
n.s.
*
-0.4
0.0
0.4
Olfactory preference index
J
Cell-specific rescue
UAS-hLRRK2
OPN>UAS-hLRRK2
hLRRK2G2019S
LRRKKO
UAS-hPINK1
OPN>UAS-hPINK1
hPINK1P399L
UAS-Rab39
OPN>UAS-Rab39
hRab39BG192R
T1 > UAS-Rab39
UAS-Aux
OPN>UAS-Aux
AuxR927G
UAS-Synj
OPN>UAS-Synj
SynjR258Q
n.s.
*
-0.4
0.0
0.4
Olfactory preference index

Figure 2. Cholinergic olfactory projection neurons are impaired across PD fly models at premotor stage. See also Figures S1-S3.

(A) t-SNE of 226k cells characterized by single cell sequencing of fly brains. Colors indicate cell types. Dopaminergic neurons (DAN), Olfactory projection neurons (OPN) and mushroom body Kenyon cells (KCs) are labeled.

(B) Fly brain, highlighting PAM DAN, OPN and KC.

(C)-(H) t-SNE of cells from six PD fly models at premotor stage. Black: cells with significant transcriptomic change. Arrows point to PAM DAN, OPN and KCs.

(I) Olfactory performance of flies at premotor stage (choice between motor oil vs. banana) of the indicated genotypes.

(J) Olfactory performance of PD model flies when wildtype gene is expressed in OPN or T1 cholinergic interneurons.

Bars indicate mean and S.E.M.. $n \geq 5$ assays, ≥ 200 flies per genotype. *, $p<0.05$ in ANOVA and Dunnett's test. Grey indicates the variance of controls.

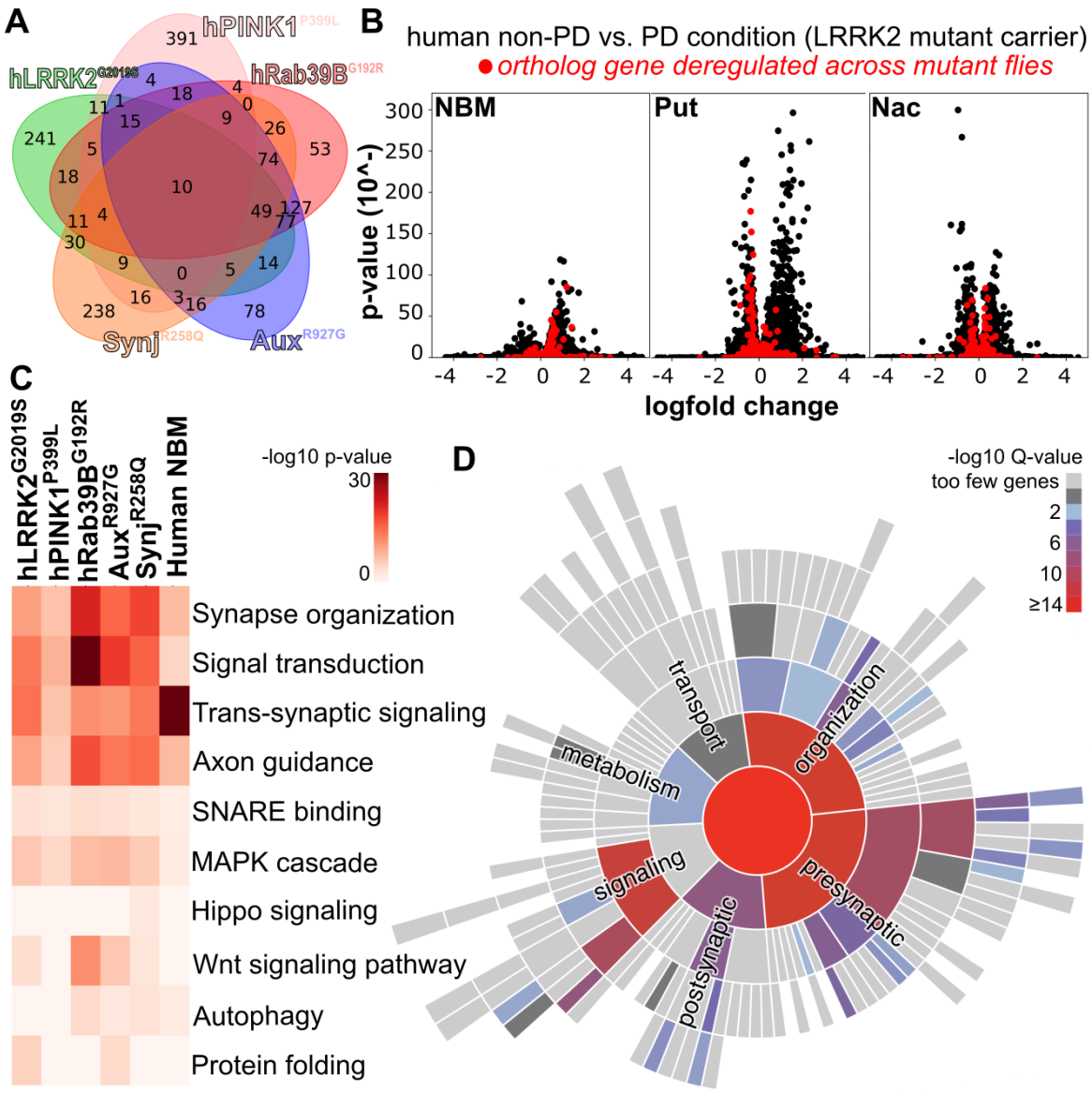

Figure 3. Common synaptic genes and pathways are deregulated in cholinergic brain regions of fly PD models and human PD patients. See also Figure S4.

(A) Venn diagram of deregulated genes (DEG) in the five olfactory impaired PD models. Green-hLRRK^{2G2019S}, pink-hPink1^{P399L}, red-hRab39B^{G192R}, blue-Aux^{R927G}, orange-Synj^{R258Q}

(B) Volcano plots of genes found in neurons in post-mortem NBM - Nucleus basalis Meynert, Put - Putamen, Nac - Nucleus accumbens of human patients carrying a LRRK2 mutation, compared to age and sex matched non-PD samples. Red: genes also found deregulated across young PD fly models.

(C) Top GO hits when analyzing DEG in cholinergic neurons of young PD fly models and NBM neurons of PD patients. Redundant terms were removed. Color indicates the adjusted p-value. **(D)** Sunburst plot generated in SynGO using the human genes deregulated both in post mortem brain samples of PD patients and in fly PD models at premotor stage.

Presynaptic function and organisation

ABI2	Abi	NLGN2	Nlg2
ACTG1	Act5C	NLGN2	Nlg3
ADGRL2	Cirl	NLGN4Y	Nlg2
ADGRL3	Cirl	NLGN4Y	Nlg3
AP1G2	AP-1gamma	OPHN1	Graf
ATP6V0B	VhaPPA1-1	PPP3CA	CanA-14F
ATP6V1H	VhaSFD	PPP3CA	Pp2B-14D
CACNA1A	Ca-alpha1D	PRKAR1B	Pka-R1
CACNA1B	Ca-alpha1D	PRKAR2A	Pka-R1
CACNA1C	Ca-alpha1D	PRKAR2B	Pka-R1
CACNA1D	Ca-alpha1D	PRKCB	Pkc53E
CACNA1E	Ca-alpha1D	RAPGEF4	Epac
CACNA2D3	Ca-Ma2d	RAPGEF5	Epac
CADPS	Cadps	RB1CC1	Atg17
CPLX1	cpx	RCAN1	sra
DSCAM	Dscam1	RCAN2	sra
DSCAM	Dscam2	RIMS3	Rim
DSCAM	Dscam4	ROBO1	robo1
EFR3B	stmA	ROBO2	robo1
ERC1	brp	SAMD5	SKIP
ERC2	brp	SASH1	SKIP
FBXL20	CG9003	SCN1A	para
HOOK1	hook	SCN2A	para
HOOK2	hook	SCN8A	NaCP60E
HSP90AB1	Hsp83	SCN8A	para
HSPA5	Hsc70-4	SH3GL2	EndoA
KCNB1	Shab	SNAP25	Snap24
KCNC2	Shawl	SNAP25	Snap25
KCNH1	eag	STXBP5	Tomosyn
KCNIP1	CG44422	STXBP5L	Tomosyn
KCNIP2	CG44422	SYT1	Syt1
KCNIP4	CG44422	SYT1	Sytalpha
KCNN2	SK	SYT2	Syt1
KCNN3	SK	SYT2	Sytalpha
LRRN1	trn	SYT7	Syt7
MAP1A	futsch	TSPOAP1	Rbp
MAPT	tau	UNC79	unc79

Postsynaptic function and organisation

ADAM10	kuz	GRID1	CG11155	MYO5A	didum
ADAM12	Meltrin	GRIK2	CG11155	NRXN3	Nrx-1
ADAM17	Tace	GRIK3	CG11155	NUMB	numb
ADAM19	Meltrin	GRM1	mtt	OPHN1	Graf
ADAM22	Meltrin	GRM3	mtt	RAPGEF1	C3G
ADAM23	mmd	GRM5	mtt	RAPGEF4	Epac
ADAM9	Meltrin	GRM8	mtt	RAPGEF5	Epac
CHRM2	mAChR-A	HPCA	Nca	RB1CC1	Atg17
CHRM3	mAChR-A	HSP90AB1	Hsp83	SNAP23	Snap24
CPLX1	cpx	HSPA5	Hsc70-4	SNAP23	Snap25
DLG1	dlg1	IQSEC1	siz	SYNE1	Msp300
GRIA3	GluRIA	IQSEC2	siz	SYT4	Syt4
GRIA3	GluRIB	IQSEC3	siz	TNIK	msn
GRIA4	GluRIA	MAP1A	futsch	TTYH3	CG3638
GRIA4	GluRIB	MAPT	tau	TTYH3	tty

RNA & metabolism

ACHE	alpha-Est9	DGKH	CG34384	PURB	Pur-alpha
ADAM10	kuz	EEF1A1	eEF1alpha2	PURG	Pur-alpha
ADAM12	Meltrin	EEF1A2	eEF1alpha2	RAB26	Rab26
ADAM17	Tace	FBXL20	CG9003	RPL29	RpL29
ADAM19	Meltrin	HNRNPK	HnRNP-K	RPL9	RpL9
ADAM22	Meltrin	MYO5A	didum	RPS16	RpS16
ADAM23	mmd	PLCB1	norpA	RPS18	RpS18
ADAM9	Meltrin	PLCB1	Plc21C	SLC16A7	hrm
DGKB	Dgk	PURA	Pur-alpha	SYNE1	Msp300

Transport

ARHGEF4	RhoGEF3	RAPGEF1	C3G
ARHGEF9	RhoGEF3	RAPGEF4	Epac
MAP1A	futsch	RAPGEF5	Epac
MAPT	tau	TIAM1	sif
MYO5A	didum	TIAM2	sif
PURA	Pur-alpha	TUBA1A	alphaTub84D
PURB	Pur-alpha	TUBA1B	alphaTub84D
PURG	Pur-alpha	TUBB	betaTub56D
RAB11A	Rab11	TUBB2A	betaTub56D
RAB26	Rab26	TUBB2B	betaTub56D
RAP1GAP	RapGAP1	TUBB4B	betaTub56D

Signaling

ADCY1	rut	GNAI2	Galphao	GUCY1A2	Gycalpha99B	PPP3CA	CanA-14F	TENM1	Ten-a
CHRM2	mAChR-A	GNAL	Galphas	HNRNPK	HnRNP-K	PPP3CA	Pp2B-14D	TENM2	Ten-a
CHRM3	mAChR-A	GNAO1	Galphao	IQSEC1	siz	PRKAR1B	Pka-R1	TUBA1A	alphaTub84D
DGKB	Dgk	GNAS	Galphas	IQSEC2	siz	PRKAR2A	Pka-R1	TUBA1B	alphaTub84D
EPHA3	Eph	GNB5	Gbeta5	IQSEC3	siz	PRKAR2B	Pka-R1	TUBB	betaTub56D
EPHA4	Eph	GRM1	mtt	KCNN2	SK	PTPRD	Lar	TUBB2A	betaTub56D
EPHA5	Eph	GRM3	mtt	KCNN3	SK	RCAN1	sra	TUBB2B	betaTub56D
EPHA6	Eph	GRM5	mtt	NRXN3	Nrx-1	RCAN2	sra	TUBB4B	betaTub56D
EPHA7	Eph	GRM8	mtt	PLCB1	norpA	SHANK3	Prosap	WLS	wls
EPHB6	Eph	GUCY1A1	Gycalpha99B	PLCB1	Plc21C	SYT4	Syt4		

Figure 4. DEG that are commonly detected across young PD fly models and cholinergic brain regions of PD patients carrying a LRRK2 mutation.

Shown are the DEG that have been annotated to synaptic function. Left column are the human genes, right columns the respective fly ortholog. Colors indicate the SynGO categories shown in Fig. 3.

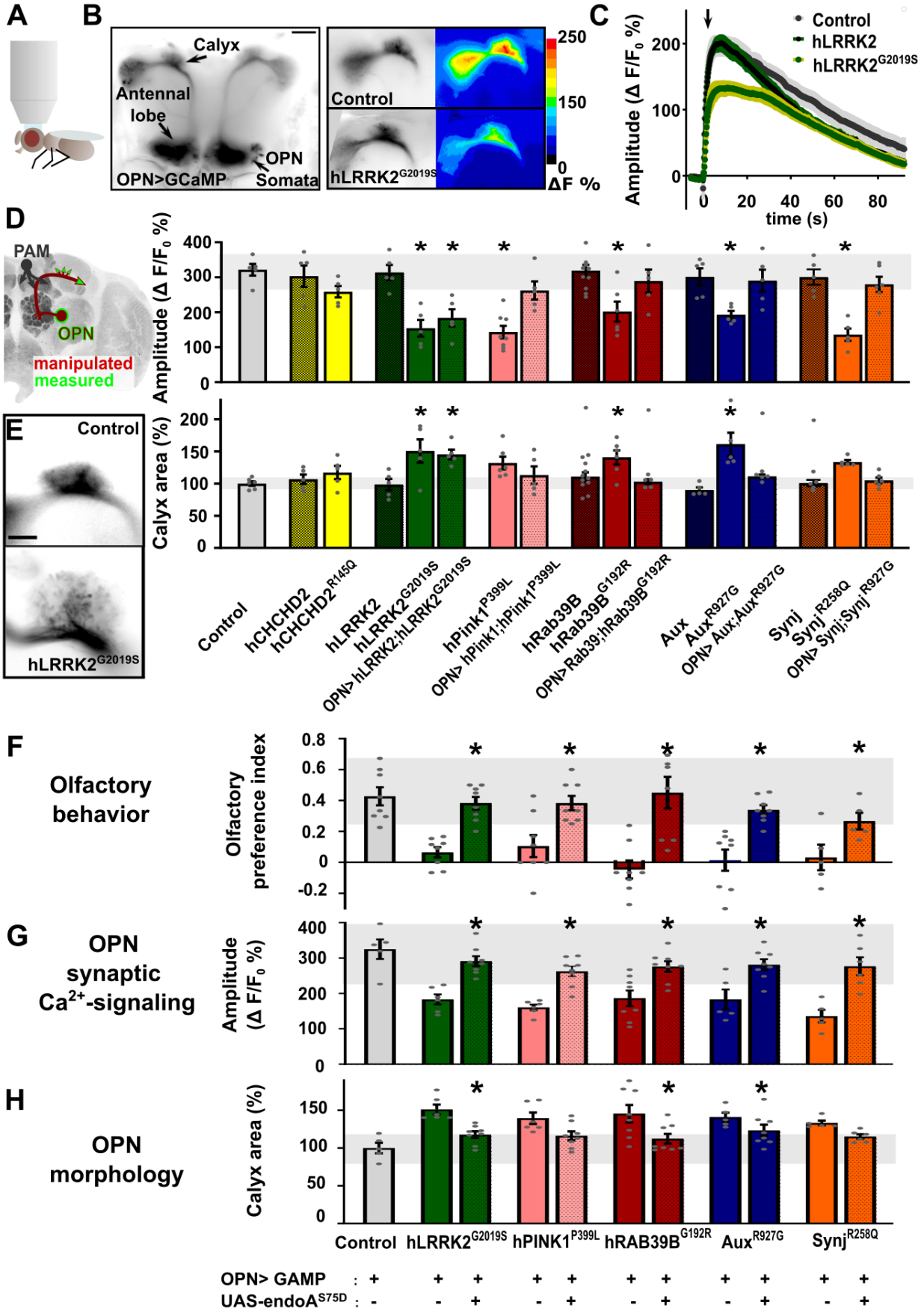
A
B
Calyx
Antennal lobe
OPN Somata
OPN>GCaMP
Control
hLRRK2G2019S
250
150
0
ΔF %
C
Control
hLRRK2
hLRRK2G2019S
Amplitude (Δ F/F0 %)
time (s)
D
PAM
OPN
manipulated
measured
Amplitude (Δ F/F0 %)
Calyx area (%)
E
Control
hLRRK2G2019S
Control
hCHCHD2
hCHCHD2R145Q
hLRRK2
hLRRK2G2019S
OPN> hLRRK2;hLRRK2G2019S
hPink1P399L
OPN> hPink1;hPink1P399L
hRab39B
hRab39BG192R
OPN> Rab39;hRab39BG192R
Aux
AuxR927G
OPN> Aux;AuxR927G
Synj
SynjR258Q
OPN> Synj;SynjR927G
F
Olfactory behavior
Olfactory preference index
G
OPN synaptic Ca2+-signaling
Amplitude (Δ F/F0 %)
H
OPN morphology
Calyx area (%)
Control
hLRRK2G2019S
hPINK1P399L
hRAB39BG192R
AuxR927G
SynjR258Q
OPN> GAMP
UAS-endoAS75D

Figure 5. Impairment of OPN synapses in PD models is rescued by synaptic autophagy. See also Figure S5.

(A) Ca^{2+} - imaging through a window in the fly's head in OPN of awake flies.

(B) GCaMP3 is expressed in OPN using GH146-Gal4 and stimulus-induced change of fluorescence is quantified in the synaptic region of the calyx. Representative example for control and $LRRK2^{G2019S}$, side-by-side with the stimulus-induced color-coded fluorescence change. Scale bar: 50 µm.

(C) Average fluorescence change (± SEM). Arrow: stimulus application.

(D) Quantification of GCaMP3 amplitude across controls and PD models with or without OPN-specific expression of wildtype CDS.

(E) Representative examples and quantification of synaptic area in the calyx across controls and PD models with or without OPN-specific expression of wildtype CDS.

$n \geq 5$ animals per genotype. *, $p<0.05$ in ANOVA, followed by Dunnett's test vs. control. Scale bar is 20µm.

(F)-(H) Olfactory behavior performance, stimulus-induced GCaMP3 amplitude in OPN synaptic area and size of OPN synaptic area across PD models with or without OPN-specific expression of phosphomimetic $endoA^{S75D}$. $n \geq 5$ per genotype. *, $p<0.05$ in ANOVA, Bonferroni corrected pairwise comparison. Bars: mean and SEM. Grey zone: variance of controls.

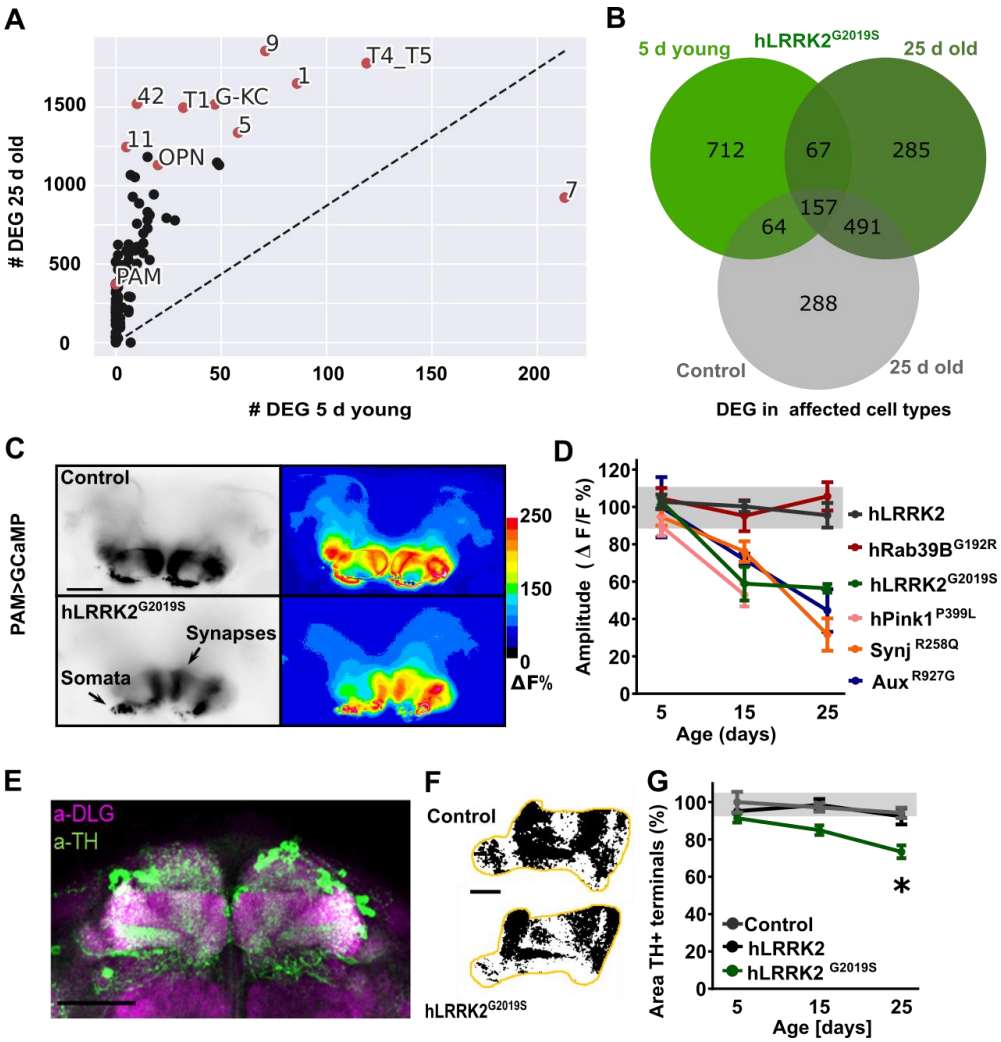

Figure 6. Age-dependent dopaminergic decline in PD model flies.

(A) Graph showing the number of DEG in young versus old LRRK2^{G2019S} knock-in mutant fly brains across cell types. Cell types that are already affected at young age are indicated in red. PAM dopaminergic neurons are also labeled; they are not affected in young animals.

(B) Venn diagram showing overlap in DEG between young and aged LRRK2^{G2019S} and aged control. DEG in brains of aged LRRK2^{G2019S} animals overlap little with DEG of aged controls.

(C) GCaMP3 is expressed in PAM dopaminergic neurons using R58E02-Gal4 and stimulus-induced change of fluorescence is quantified in the synaptic region of the mushroom body lobes. A representative example is shown for control animals and LRRK2^{G2019S} knock-ins, side-by-side with the stimulus-induced color-coded fluorescence change. Scale bar is 50µm.

(D) Quantification of fluorescence change upon stimulation in PAM dopaminergic neuron terminals of PD fly models at different ages. Ca^{2+} responses are significantly reduced from day 15 onwards in all PD models except hRab39B^{G192R}. n=6 animals per genotype and time point.

(E) Maximum intensity projection of confocal imaging of the mushroom body lobes in the anterior fly brain labeled with the dopaminergic marker anti-TH (green) and the synaptic marker anti-DLG (magenta).

(F) Quantification of TH-immunoreactive area (black) within the mushroom body lobes, examples are of 15-day old flies.

(G) TH-immunoreactive area within the mushroom body lobes in controls and LRRK2^{G2019S} at different ages. Mean and SEM. $n \geq 5$, *- $p<0.05$ for genotype in 2-way-ANOVA. Grey zone: variance of controls.

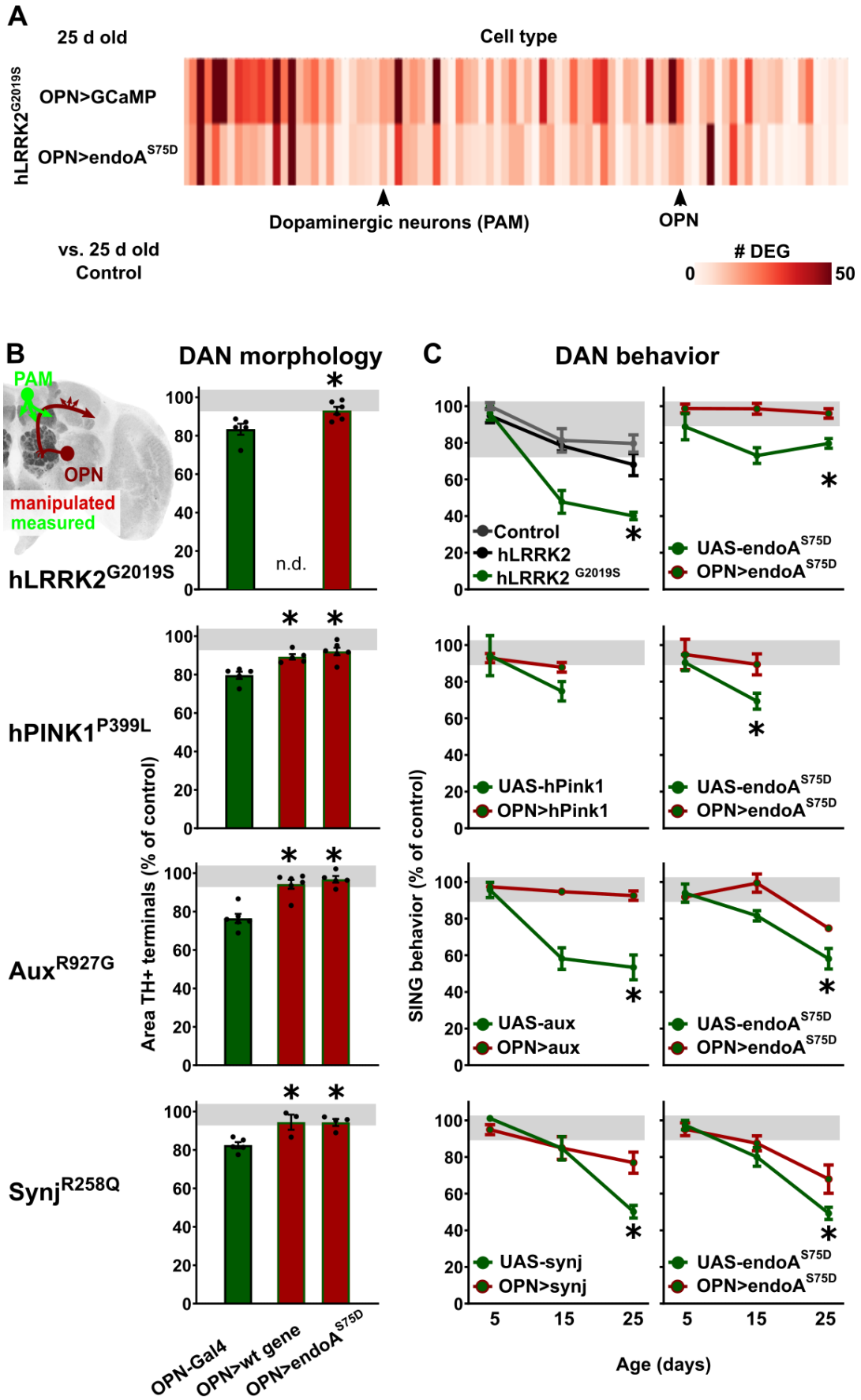
A
25 d old
Cell type
hLRRK2G2019S
OPN>GCaMP
OPN>endoAS75D
Dopaminergic neurons (PAM)
OPN
vs. 25 d old Control
DEG
0
50
B
DAN morphology
PAM
OPN
manipulated
measured
hLRRK2G2019S
n.d.
hPINK1P399L
AuxR927G
SynjR258Q
Area TH+ terminals (% of control)
OPN-Gal4
OPN>wt gene
OPN>endoAS75D
C
DAN behavior
Control
hLRRK2
hLRRK2 G2019S
UAS-endoAS75D
OPN>endoAS75D
UAS-hPink1
OPN>hPink1
UAS-aux
OPN>aux
UAS-synj
OPN>synj
SING behavior (% of control)
Age (days)

Figure 7. Restoring OPN function prevents age-dependent decline of DAN function across PD models.

(A) Heatmap of transcriptomic changes across cell types in aged LRRK2^{G2019S} knock-ins that express either GCaMP (top) or endoA^{S75D} (bottom) in OPN when compared to aged (25d old) controls. OPN and dopaminergic neurons are indicated. Dark red represents high amount of DEG.

(B) Synaptic area of DAN innervating the mushroom body in aged PD models and with or without OPN-specific expression of wildtype gene or endoA^{S75D}. Bars: mean and SEM. $n \geq 5$, *- $p<0.05$ in ANOVA, Dunnett's test.

(E) SING of PD models with or without OPN-specific expression of wildtype gene or endoA^{S75D}. Mean and SEM. $n \geq 5$, *- $p<0.05$ for genotype in 2-way-ANOVA. Grey zone: variance of controls.

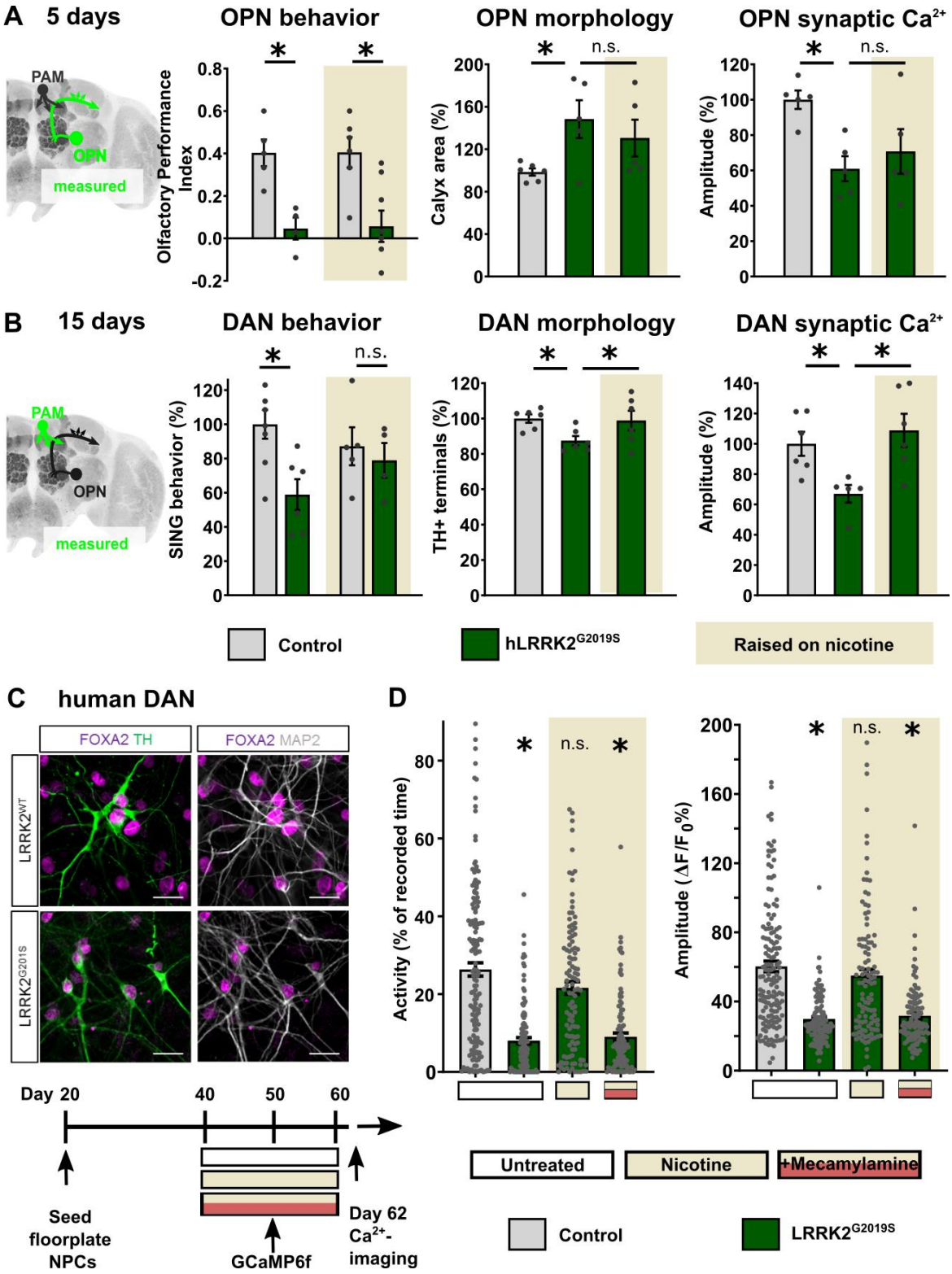

Figure 8. Chronic application of nicotine rescues human and fly DAN. See also Figure S6.

(A) Odor choice performance, stimulus-induced changes in synaptic Ca^{2+} and OPN synapse area of young PD models with or without chronic application of nicotine. Bars: mean and SEM. n≥5 assays, *- p<0.05 in ANOVA, Dunnett's test.

(B) Performance in SING, stimulus-induced changes in synaptic Ca^{2+} and DAN synapse area of aged PD models with or without chronic application of nicotine. Bars: mean and SEM. n≥5 assays, *- p<0.05 in ANOVA, Dunnett's test.

(C) Confocal images of differentiated (60 days) wildtype and LRRK2 ^{G2019S} ventral midbrain DAN labeled with the ventral midbrain marker FOXA2, dopaminergic marker TH and neuronal marker MAP2. Scale bar: 20 µm. Scheme: treatment protocol.

(D) Spontaneous Ca^{2+} activity and amplitude of induced DAN 2 days after a 20-day treatment with nicotine or nicotine and nAchR-blocker mecamylamine. Bars: mean and SEM. n≥60 DAN, 3 independent differentiations, *- p<0.05 in ANOVA, Dunnett's test.

STAR Methods

Resource availability

Lead contact
For further information and requests for resources and reagents contact Patrik Verstreken (patrik.verstreken@kuleuven.be).

Material availability
Plasmids and fly lines generated in this study are available on request.

Data and code availability
Codes and data sets generated in this study will be stored online and available upon publication.

Experimental model details

The "control" we refer to is a semi-isogenized w^{1118} backcrossed to CantonS for 10 generations (cantonized *w*). We sequenced the entire genome of the resulting fly line and defined there are no deleterious mutations in homologues of known causative Parkinson's disease genes or in homologues of human genes located close to GWAS loci. All our knock-ins (see below), UAS (see below) and Gal4 lines were backcrossed for >10 generations to this control. All generated fly lines were verified by multiple PCRs and PCR-product sequencing.
Flies were reared on standard yeast food medium at 25° C and kept on 12/12 h light/dark cycles. Flies were kept in mixed populations of analogous density and were flipped onto fresh food every three days. Brains for RNA experiments, including single cell sequencing, were dissected between 11 and 12 h Zeitgeber time, behavioral and physiology experiments were performed between 18 and 20 h Zeitgeber time. Males and females were tested together, quantified separately, and results pooled if there was no statistical difference. Male hPINK1 pathogenic mutant knock-in flies are sterile, requiring balancing of the stock and consequently they produce only male hemizygotes to be quantified in experiments.

Generation of *Drosophila* PD models

A complete list of primers, oligos, gBlocks and fly strains used will be provided. To clone inserts into plasmids NEBuilder® HiFi DNA Assembly (NEB) was used.
Unique gRNAs (file S1) for *CHCHD2*, *LRRK2*, *PINK1*, *Rab39B*, *Aux* and *Synj* were identified by http://crispr.mit.edu/ and introduced into pCFD4: U6:1-gRNA U6:3-gRNA (Port et al., 2014) by following an established protocol: http://www.crisprflydesign.org/wp-content/uploads/2014/06/Cloning-with-pCFD4.pdf.
Homology arms of 1kB surrounding the first common exon of the different transcripts from the gene of interest were cloned into pWhite-STAR[62]. For *Aux*, homology arms surrounded the entire *Aux* gene. HiFi DNA Assembly (NEB) was performed with four fragments: mini-white IMCE-cassette, left homology arm, right homology arm and the plasmid backbone. The homology arms were either generated by gBlocks (IDT), which were modified in order to make them compatible with the requirements of IDT, or amplified by Q5 PCR from genomic fly DNA of the target genotype (CantonS *w*). The mini-white IMCE-cassette and vector backbone were generated by restriction digest on pWhite-STAR[45] with AvrII and XhoI. In order to avoid cutting of the donor plasmid, the PAM sequence of the target was mutated, if located in the homology arms. Mostly NGG to NAA modifications were used, however different modifications were used when necessary (presence of PAM in coding region). The donor plasmids pDoC-miniwhite-gene (Donor cassette) contains an Integrase mediated exchange (IMCE) cassette surrounded by two homology arms that allows for HDR (homology directed repair). HDR occurs when two double strand breaks are introduced in the DNA surrounding the first (or second) common exon of all transcripts. This HDR replaced the first common exon by the IMCE-cassette. Site of HDR was directed by the choice of the homology arms in a way such that the two attP sites for IMCE were situated inside evolutionary non-conserved regions.
Rescue plasmids were used to exchange the mini-white IMCE-cassette with the coding DNA sequence (CDS) of target genes. All rescue plasmids contain: 1. a stretch of genomic sequence that will be referred to as 'utr': this sequence was deleted together with the removed exon of the target gene and now is being placed back to repair the locus; 2. CDS of the target gene and 3. a poly(A)-tail. These 3 elements are surrounded by two attB sites. The rescue plasmids are named pReC-*gene* or pReC2-*gene* and are target gene-specific. The backbone: pReC was generated by linearizing pUC19 with SapI and EcoRI followed by insertion of two gBlocks: attB-MCS-L and MCS-attB-R. We also created pReC2, an optimized version that allows for easier cloning of the utr and CDS as it already contains the SV40 poly(A), by linearizing pUC19 with SapI and EcoRI followed by insertion of two gBlocks: attB-2xMCS-L and 2xMCS-attB-R.

CHCHD2: pReC was linearized with SapI. Two fragments containing the utr and a SapI restriction site (for subsequent cloning of the CDS and poly(A)) are generated from genomic fly DNA by Q5 PCR with primers F_5'UTR_CHCHD2, R_5'UTR_CHCHD2 and F_3'UTR_CHCHD2, R_3'UTR_CHCHD2 and cloned into pReC. The resulting plasmid was linearized with SapI. gBlocks containing the human $CHCHD2^{WT}$ and $CHCHD2^{T61I}$ CDS were introduced into the linearized plasmid. The resulting plasmids are pReC-hCHCHD2 and pReC-hCHCHD2T61I. pReC-hCHCHD2R145Q was created by using Q5® Site-Directed Mutagenesis (NEB) with primers F_mut_CHCHD2_R145Q, R_mut_CHCHD2_R145Q on pReC-hCHCHD2.

LRRK2: pReC was linearized with SapI. gBlock LRRK2:utr-P2A-SapI-SV40, containing the utr a P2A site (since we knocked-out exon 2), SapI restriction site (for subsequent cloning of the

CDS) and an SV40 poly(A)) was introduced. The resulting plasmid was linearized with SapI. Next the CDS of *LRRK2* was amplified from 2XMyc-LRRK2-WT with F_hLRRK2_cDNA and R_hLRRK2_cDNA and introduced into the linearized plasmid. The resulting plasmid is called pReC-hLRRK2. pReC-hLRRK2G2019S and pReC-hLRRK2Y1699C were created by using Q5® Site-Directed Mutagenesis (NEB) with primers F_mut_LRRK2_G2019S, R_mut_LRRK2_G2019S and Fmut_LRRK2_Y1699C, R_mut_LRRK2_Y1699C respectively on pReC-hLRRK2.

PINK1: pReC was linearized with SapI. gBlock: PINK1:utr-SapI containing the utr and SapI restriction site (for subsequent cloning of the CDS) is cloned into pReC. The resulting plasmid was linearized with AflIII. Next, the gBlock PINK1:SV40poly(A) containing the human Sv40 poly(A) was introduced into the linearized plasmid. This plasmid is linearized with SapI. Next the CDS of human *PINK1* was amplified from pLenti6-DEST PINK1-V5 WT with F_hPink1_cDNA and R_hPINK1_cDNA and introduced into the linearized plasmid. The resulting plasmid is called pReC-hPINK1. pReC-hPINK1R145Q and pReC-hPINK1L347P were created by using Q5® Site-Directed Mutagenesis (NEB) with primers F_mut_PINK1_L347P, R_mut_PINK1_L347P and F_mut_PINK1_P399L, R_mut_PINK1_P399L respectively on pReC-hPINK1. While we created wildtype CDS knock ins for rescue experiments of all Parkinson's disease models, *Pink1* we used the expression of human *PINK1* with UAS-hPINK1 and nsyb-Gal4. This is because, unlike the two pathogenic variants, we were unsuccessful in targeting the wild type human *PINK1* CDS to the fly *pink1* locus.

Synj: pReC was linearized with SapI. gBlock Synj_utr-SapI containing the utr and SapI restriction site (for subsequent cloning of the CDS) is cloned into pReC. The resulting plasmid was linearized with AflIII. gBlock Synj:SV40poly(A) containing the human Sv40 poly(A) was introduced into the linearized plasmid. This plasmid is linearized with SapI. Next the CDS of *Drosophila synj* and *synj*^{R258Q} were amplified from respectively UAS-Synj+ and UAS-SynjRQ (Vanhauwaert et al., 2017) with FW Synj and RC Synj and are introduced into the linearized plasmid by utilizing HiFi assembly. The resulting plasmids are called pReC-dSynj and pReC-dSynjR258Q.

Rab39B: pReC2 was linearized with XhoI and XbaI. A gblock: Rab39_utr was inserted into the pReC2. Next this plasmid was linearized with SapI and a gBlock containing the human *RAB39B* CDS was cloned. The resulting plasmid is called pReC2-hRab39. pReC2-hRab39T168K and pReC2-hRab39G192R were created by using Q5® Site-Directed Mutagenesis (NEB) with primers F_mut_hRab39_T168K, R_mut_hRab39_T168K and F_mut_hRab39_G192R, R_mut_hRab39_G192R respectively on pReC2-hRab39.

Aux: The entire *Drosophila auxilin* gene region was cloned from BAC CH322-22D05 into pRec using BbsI, with an HA-tag at the N-terminal of the gene. AuxR927G was produced by Q5® Site-Directed Mutagenesis (NEB). See also [63]

UAS-aux: pUAST.attB was linearized with XhoI and XbaI; gBlock: Aux was cloned into the this plasmid. See also [63]

UAS-endoA^{S75D}: pUAST.attB was linearized with EcoRI-XhoI. gBlock: EndoA-^{S75D} was cloned into the linearized plasmid.

Constructs were injected in house or by BestGene (BestGene Inc, CA, US).

Quantitative RT-PCR

For each sample, 20 heads of 5 d old males were collected, RNA was extracted and transcribed using Maxwell RSC instrument and Maxwell RSC RNA kit (Promega) and quantified by subsequent qPCR using a LightCycler 480, 480 SYBR Green master mix (Roche).

Survival assay

Flies were collected into populations of 10 males and 10 females the day after eclosion. Five days after eclosion, these populations were transferred into vials containing 1% agarose for wet starvation. Dead flies were scored and removed every 8 h, the remaining flies were flipped on fresh agarose every 24 h. The assay was repeated with at least two different batches of a given genotype. Median survival and survival curves were determined using GraphPad Prism.

Mitochondrial membrane potential (TMRE) assay

Measurements of mitochondrial membrane potential were performed with the potentiometric dye tetramethylrhodamine ethyl ester (TMRE). Male third-instar larvae were dissected in HL3 (in mM: 110 NaCl, 5 KCl, 10 MgCl2 • 6H2O, 10 NaHCO3, 30 sucrose, 5 trehalose, and 10 HEPES, pH 7.2). Larval fillets were incubated for 15 min in the presence of 50 nM TMRE (Abcam). Subsequently, the TMRE solution was discarded and fillets were rinsed three times with normal HL3 without TMRE. Mitochondrial labeling of TMRE was imaged on a Nikon spinning disk confocal microscope with a 40x water dipping objective 0.8 NA, excitation wavelength of 561 nm and an emission filter 595/50 nm. We imaged at 0.5 μm Z-steps entire NMJ branches. Larvae were stained a mutant and control larva were processed and imaged side-by-side. TMRE labeling intensity was quantified in individual synaptic boutons using Fiji [64].

Electroretinograms (ERG)

ERGs were recorded as previously described [65] . Flies were immobilized on glass microscope slides, by use of liquid Pritt glue. For recordings, glass electrodes (borosilicate, 1.5 mm outer diameter) filled with 3 M NaCl were placed in the thorax as a reference and on the fly eye for recordings. Responses to repetitive 1s light stimuli were recorded using Axosope 10.7 and analyzed using Clampfit 10.7 software (Molecular Devices) and Igor Pro 6.37. To assess the ERG response after exposure to constant light, 3-day-old flies were placed under continuous illumination (1300-lux) for 7 days at 25 C prior to ERG data acquisition as described.

Startle-induced negative geotaxis

Geotaxis locomotion was quantified in mixed populations of ~20 flies as described by Benzer, 1967 [66] with modifications described by Inagaki et al., 2010 [67]. Flies were flipped into the apparatus without anesthesia and allowed to adjust for some minutes to experimental environment (24 C, 50% humidity). They were tapped down into the first lower tube and allowed to climb into the upper tube for 30 sec, at which time the flies that reached the upper tube were

moved to tube 2. The procedure was repeated five times and the SING scored: (#flies in tube 1 + (#flies in tube 2 * 2) + (#flies in tube 3 * 3) + (#flies in tube 4 *4) + (#flies in tube 5 * 5))/(#total flies *5).

Modeling to define the number of cells to be sequenced

We randomly sampled between 0 and 50,000 cells, in steps of 100, from the annotated Davie et al. 2018 brain cell dataset [28]. For each sample we calculated the number of cell types that were retrieved for different thresholds of detection. This process was repeated 50 times for convergence and Michaelis-Menten kinetics were fit through the data points.

Brain dissection for single cell sequencing

30 fly brains (15 females and 15 males, except *Pink1* mutants, where only males were used) were dissected on ice and collected in 100 µl ice cold DPBS solution, centrifuged at 800 x *g* for 5 min, and placed into 50 µL of dispase (3 mg/mL, Sigma-Aldrich_D4818-2mg) and 75 µl collagenase I (100 mg/mL, Invitrogen_17100-017). Brains were dissociated in a Thermoshaker (Grant Bio PCMT) for 2 h at 25 C and 500 rpm. The enzymatic reaction was reinforced by pipetting every 15 min. Subsequently, cells were washed with 1000 µl ice cold DPBS solution and resuspended in 400 µl DPBS 0.04 % BSA. Cell suspensions were passed through a 10 µM pluriStrainer (ImTec Diagnostics_435001050), cell viability and concentration were assessed by the LUNA-FL™ Dual Fluorescence Cell Counter, and cells were immediately used for the 10x run.

10xGenomics high-throughput sequencing

Before sequencing, the fragment size of every library was analyzed on a Bioanalyzer high sensitivity chip. The libraries were diluted to 2 nM and quantified by qPCR using primers against p5-p7 sequence. 10x libraries were sequenced twice: shallow on NextSeq500 (Illumina) to determine library quality and more in depth using NovaSeq6000 (Illumina). The targeted saturation for each sample was around 60%, and additional sequencing runs were performed if needed. Each sequencing run used the following sequencing parameters: 28 bp read 1 – 8 bp index 1 (i7) – 91 bp read 2.

10x Data Preprocessing

The 10x fly brain samples were each processed (alignment, barcode assignment and UMI counting) with Cell Ranger (version 3.0.2) count pipeline. The Cell Ranger reference index was built upon the 3rd 2017 FlyBase release (*D. melanogaster* r6.16) [68]. To count the human mutated genes, sequences from the construct were added as artificial chromosomes to the index. For every sample all sequencing runs were aggregated using CellRanger and the *–recovered-cells* parameter was specified as 5000.

Data filtering and clustering

CellRanger generated a gene expression matrix, which was used as input for VSN pipelines[69] for the first filtering and data clean up. These pipelines are written in Nextflow DSL2 making them

highly reproducible, and the config file used for the fly samples can be found in Supplementary File X. The VSN pipeline removed predicted doublets using scrublet [70], followed by a cleaning of ambient RNA reads using DecontX [71], similar to the procedures used in the Fly Cell Atlas [72].

Afterwards the data was loaded into scanpy (1.8.2, [73]). Cells were filtered using min_genes=200, max_genes=7000, min_counts=500 and max_counts=30000, and finally with percentage of mitochondrial counts below 15. The data were log-normalized with a scale factor of 10^4 and scaled (maximum values = 10), regressing out the number of UMIs and the percentage of mitochondrial genes as latent variables using a linear regression model. Highly variable genes were selected using sc.pp.highly_variable_genes with default parameters.

We used sc.tl.pca to calculate 250 principal components on the highly variable genes, from which the first 100 components were selected for follow-up analysis based on an elbow plot. Since the data contains many samples (n=65) covering a variety of different ages and genotypes, we noticed batch effects and low mixing with default parameters. Therefore, we used Harmony [ref] to correct the principal components. For this we used sce.pp.harmony_integrate with max_iter_harmony=20, using the genotype + age combination as batch variable. The batch effect-corrected components were then used as input to calculate neighbors using sc.pp.neighbors with n_neighbors=30, followed by Leiden clustering for resolutions between 2 and 20. Subsequently, tSNE and UMAP visualizations were calculated.

Seurat

Dimensionality reduction and clustering were performed using the Seurat package in R [74]. The processed and filtered matrices of all samples were combined together with an annotated dataset of 57k cells of the adult brain containing two wild type genotypes [28], leading to a total number of ~170k cells. In the first steps of the Seurat pipeline, each genotype was processed separately. The data were log-normalized with a scale factor of 104 and scaled, regressing out the number of UMIs and the percentage of mitochondrial genes as latent variables using a negative binomial model. For further downstream analysis, the 2000 most variable genes were selected using FindVariableGenes and method='vst' with default parameters. Then 3000 integration features were determined across all genotypes with SelectIntegrationFeatures and used in the rest of the analysis. At this point we looped over a number of components to test the dimensionality of the dataset, ranging between 30 and 100 components. These components were used as input for the integration functions, PCA, tSNE and clustering. Integration was performed by linking cells between datasets (so-called anchors, function FindIntegrationAnchors), followed by integrating the datasets one by one (IntegrateData). The scaled and integrated matrix was used as input for PCA to reduce the dimensions. The principal components were then used to calculate the non-linear dimensionality reduction tSNE (RunTSNE), and to perform clustering with Louvain Shared-Nearest Neighbor (SNN) graph algorithm (FindNeighbors, FindClusters). Different resolutions ranging between 1 and 8 were tested. In general, results are only slightly affected by the number of components used (Seurat tutorial), so we decided to compare the tSNE and clusters qualitatively, settling on 70 as the final number.

Label transfer

In the previous step different resolutions were used in clustering, leading to an increasing number of clusters detected. To start annotating these and to find a final clustering resolution, we compared the detected clusters with the annotations from the co-clustered published dataset [28; 73] and annotations from the Fly Cell Atlas [72]. In addition, we also used the neural net classifier from Özel et al. [28] using default parameters as described. Finally, we compared the clusters with sorted cell types from Davis et al. [75] using lasso regression as described below. These data were used to annotate clusters in resolution 20, after which clusters with the same annotation were merged. For unknown cells, we chose to use Leiden resolution 5 as basis annotation to not split clusters too much and keep enough cells to perform meaningful differential expression analysis.

In total we found 188 clusters, of which 83 were annotated (median size = 1,011 cells, total = 140,778 cells) and 105 unknown (median size = 810 cells, total = 145,010 cells).

Lasso regression

To expand the published atlas, we analysed the bulk transcriptomes of multiple FAC-sorted neuronal cell types [28]. Regression models have been previously used to compare bulk transcriptome profiles to aggregated cluster profiles, including non-negative least squares [28]. Here we use lasso regression to predict single cell cluster transcriptome profiles using the bulk profiles as variables. Therefore, each single cell cluster is decomposed as a weighted sum of bulk profiles. The regularization of the lasso model, allows for a higher signal to noise ratio and clearer assignments. Clear matches between a cluster and a bulk profile are detected as high coefficients (>0.1) in the sum. The regression model was fit using gene signatures derived from Seurat as features. Before fitting, all datasets were scaled to counts per million CPM using the common genes, independent of previously applied normalization techniques. The calculations were performed using the SciPy [76] and Scikit-learn packages in Python.

Human brain samples

Usage of post-mortem brain samples was ethically approved (EC reference NH019 2019-02-01). All tissue samples were obtained from the Parkinson's UK Brain Bank at the Imperial College London. The Parkinson's disease cases used in this study all carried a mutation in the *LRRK2* gene (P1542S, M1646T or R1325Q). One case carried a mutation in *PARKIN* in addition and one case carried a mutation in *EIF4G* in addition. Control samples are from cases without pre- or post mortem Parkinson's disease-associated pathology and diagnosis.

Human nuclei isolation

Nuclei of human samples were prepared as described in Slyper et al., 2020 [77].

Calling SNPs

In the human data, 10 different genotypes (5 PD cases, 5 controls) were mixed across 3 regions. To perform demultiplexing, the SNPs are required per sample. Since no genotype information was available, we performed bulk RNA-seq on all samples and called SNPs on the

transcriptome. For this we used BCFFtools (v1.11, [72]). We performed a pileup using the common loci of the 1000 Genomes project [68; 78] on the Hg38 iGenomes genome (-d 8000, -Ou), calling SNPs with the bcftools call function (-mv, -Ob). Using the reheader function we then updated the bcf file to make it compatible with demuxlet. We detected 146,848 SNPs, ranging between 25K and 51K per genotype (see table). Next, the bcf file was sorted in the same order as the bam files and bcftools +fill-tags was used to add frequencies.

Genotype	SNPs
C23	25,222
C45	41,379
C72	37,607
C73	40,651
C87	48,896
PD106	38,281
PD188	62,987
PD194	46,071
PD348	44,195
PD423	51,902

Demuxlet

Bam files were filtered using SAMtools (1.11, [72]) to only contain reads overlapping with the vcf file. Then popscle dsc-pileup was used to create a pileup file for input in popscle demuxlet [79]. All cells labeled as doublets were removed (~4-7%), and cells assigned to singlets were kept (25-43%). Additionally, a large proportion of cells (~49-69%) were labelled as ambiguous. These cells were assigned to their most likely singlet identity and kept in the remaining analysis. In a next step, we only kept possible genotype-experiment combinations, ending up with 97,489 cells.

Data filtering and clustering

CellRanger generated a gene expression matrix of 151,368 cells. After removing doublets and wrongly assigned cells, 97,489 cells remained. The data was loaded into scanpy (version, ref) and further filtered using min_genes=500, max_genes=7000, min_counts=1000 and max_counts=30000, and finally with percentage of mitochondrial counts below 5. We lowered the allowed percentage of mitochondrial counts since the human data was obtained from snRNA-seq. The data were log-normalized with a scale factor of 10^4 and scaled (maximum values = 10), regressing out the number of UMIs and the percentage of mitochondrial genes as latent variables using a linear regression model. Highly variable genes were selected using sc.pp.highly_variable_genes with default parameters.

We used sc.tl.pca to calculate 200 principal components on the highly variable genes, from which the first 75 components were selected for follow-up analysis based on an elbow plot. We again used Harmony [ref] to correct the principal components for batch effects. The batch effect-corrected components were then used as input to calculate neighbors using sc.pp.neighbors with n_neighbors=30, followed by Leiden clustering for resolutions between 1 and 10. Subsequently, tSNE and UMAP visualizations were calculated.

Using marker genes for main neuronal and glial populations we chose to combine Leiden resolution 1 for glia and Leiden resolution 3 for neurons.

Gene set enrichment was performed using the AUCell function from the pyscenic package (0.10.4) in Python. The genes detected in affected cell types of *Drosophila* models were converted to human homologues using the FlyBase database, selecting homologues with a DIOPT score>=5. Significant enrichment was determined using a two-tailed t-test.

Differential expression

For every cluster, cells from each mutant genotype were compared against cells from the wild-type control. In the fly, OPN subtypes were merged before calculating differential genes (DEG). To control for biases in methods, we used Wilcoxon and DESEQ2 [80]. The Wilcoxon test was performed with the scanpy wrapper sc.tl.rank_genes_groups. For DESEQ2 we used rpy2 to call the R package DESEQ2 in Python. DESEQ2 was originally designed to be used on bulk RNA-seq data. Therefore, we grouped cells into pseudobulks based on their experimental run by summing their gene expression profiles. Only pseudobulks consisting of at least 10 cells were kept. We did not select any additional variables to regress.

To detect any method biases, we calculated the spearman correlation of the signed p-value (log-foldchange multiplied with log(p-val)), showing that both methods differ in the exact number of DEG, but agree quite well in their ranking of up- and downregulated genes. We found larger differences in the number of DEG called in the human data (0-10 in DESEQ2, 200-1800 in Wilcoxon) but the rankings remained highly correlated (r~0.8). The Wilcoxon test is more sensitive to genes expressed in all cells in the cluster, while DESEQ2 can be oversensitive to genes expressed in only a minor fraction of cells.

Additional runs were made in which the number of cells per cluster was down sampled to correct against cluster-size based biases.

Modeling of DEGs

Since the number of DEG has been shown to be highly correlated with the number of cells in single-cell RNA-seq, we used a modeling approach to find outlier clusters with more than expected DEG. Since the data is over dispersed count data, we fit a negative binomial model to the data, with number of differential genes (nDEG) as dependent variable and number of cells in the mutant and number of cells in the control as independent variables:

$$E[y_i|\alpha,\mu_i] = \mu_i$$
$$VAR[y_i|\alpha,\mu_i] = \mu_i + \alpha{\mu_i}^2$$
$$\log(\mu_i) = Intercept + B_1 * \log(\min(X_{1i}, X_{2i}))$$

With y_i being the number of differential genes detected in cluster i, $X_{1i}$the log of the number of cells of cluster i in the mutant and X_{2i} the number of cells of cluster i in the wild type.

Models were fit using the statsmodels package in Python and goodness of fit was measured using the Log-Likelihood (summaries in file S3). The number of UMIs per cluster was not included as

independent variable, since it has been implicated with cell size and thus could remove biological effects. Residuals were calculated as the difference between the measured number of differential genes and the predicted number, wherein a positive residual means that the cluster has more differential genes than expected.

$$r_i = \widehat{\mu_i} - y_i$$

Olfactory behavior assay

Olfactory behavior was quantified in mixed populations of ~50 4-6 day old flies. Flies were flipped into the experimental setup without anesthesia and allowed to adjust for some minutes to the experimental environment (24 C, 50% humidity). They were placed into a custom-built T-Maze (modified from [81]) where they were allowed to freely walk between two tubes for one minute. Throughout the test, an aquarium pump delivers two separated, constant airstreams (1 l/min) which are directed through an odor vial before entering the tube. Odor vials contained: 2 ml motor oil, 2 g fresh banana, 2 ml undiluted beer (Jupiler), or 2 ml wine (LesTruffiers, 2015) diluted 1:1000. Afterwards the olfactory preference index was scored: (#flies in tube with odor A - #flies in tube with odor B)/#total flies. Tests were pseudo-randomized by switching the position of odor tubes every trial. Control flies were tested each experimental session.

In vivo Ca^{2+}-imaging and synaptic area

4-6 day old (unless noted otherwise) male flies were placed into a custom-build chamber and the brains were imaged at 5 Hz through a window in the head capsule using a wide field fluorescence microscope (Nikon) equipped with a Hamamatsu camera and a 20×/NA=0.9 water-immersion objective. 100 mM nicotine was injected into the Ringer's solution covering the brain (final concentration ~10 mM). Images were analyzed using Fiji (Schindelin et al., 2012). Fluorescence intensity was quantified in a region of interest (ROI, d=10 µm) that was placed in the center of the synaptic area (calyx for OPNs, mushroom body lobes for dopaminergic PAM neurons) and normalized by subtracting background fluorescence. Basal fluorescence F_0 in the synaptic region was determined by averaging five frames before stimulus onset and the change of fluorescence over time was calculated by $F\text{-}F_0/F_0$. Flies of related genotypes and controls were always measured within the same sessions, in alternating order.
The area of the calyx was determined by measuring the (2D) surface of the entire visible fluorescent area.

Immunohistochemistry

Brains were dissected on ice and fixed for 2 h in 4 % paraformaldehyde (in 1x PBS) at 4 C. After 3x 20min in PBTriton 0.02% at room temperature on a shaker, they were incubated in blocking solution (freshly prepared: PBT, 1 % BSA, 5 % normal goat serum) for 2 h at 4 C. Primary antibodies were applied at 4 C for 1.5-2 days: rabbit α-TH, Sigma, 1:200, mouse α-DLG, DSHB, 1:100, or chicken α-GFP, aves labs, 1:500 in blocking solution and subsequently washed 3x 20 min in PBT with 1 % BSA at room temperature on a shaker. Secondary antibodies: goat α-rabbit Alexa488, goat α-chicken Alexa488 or goat α-mouse Alexa555, all at 1:500 in PBT with

1 % BSA were applied overnight at 4 C, brains were finally washed 6x20 min in PBT at room temperature on a shaker and mounted, anterior facing up in Vectashield (Vector labs). Z-stacks of entire brains were imaged at a Zeiss Examiner 8, using an 20x0.8 air objective and laser power and imaging parameters that are kept constant over different imaging sessions and samples. Fiji[46] was used for image analysis. Dopaminergic neurites were quantified as follows: Anti-DLG was used to define and set the synaptic region of the mushroom body lobes. Within this region, the area occupied by anti-TH fluorescence was measured automatically, using the threshold function in Fiji. Absolute area values and relative values (normalized to mushroom body lobe size) both lead to the same results in statistical comparisons. Anti-GFP labels GCaMP and was quantified in flies expressing GCaMP in OPNs within the region of interest used for Ca^{2+} - imaging (in the center of the calyx).

Electron microsocopy

Fly brains were dissected on ice and fixed in 2 % paraformaldehyde and 2 % glutaraldehyde in 0.1 M Na-Cacodylate buffer (pH 7.4) for 2 h at room temperature. Samples were further fixed at 4 C overnight, and then washed with 0.1 M Na-Cacodylate, pH 7.4, and subsequently osmicated with 2% osmium (OsO4/Na-Cacodylate buffer). After dehydration in an ascending series of ethanol solutions and staining in 2% aqueous uranyl acetate solution the specimens were embedded in Agar 100 (Laborimpex; Agar Scientific). Ultrathin sections (70 nm) of the posterior brain were collected on grids (Laborimpex; Agar Scientific) coated with Butvar and imaged on a JEM 1400 transmission electron microscope (JEOL) at 80 kV with a bottom mounted camera (Quemasa; 11 megapixels; Olympus). The calyx was identified by the characteristic outline of this neuropil. The area of individual electron-dense presynaptic T-bars was quantified in boutons within the calyx. All T-bars in several boutons were analyzed.

Nicotine treatment

Nicotine (N3876, Sigma) was mixed with fly food to reach a final concentration of 0.2µl/ml. A fly weighs ~0.1mg [82] and consumes ~1µl food a day [83]. This corresponds to 0.002 µg nicotine uptake per mg body weight daily and corresponds to the estimated amount a smoker absorbs with 10 cigarettes a day. Fly vials containing nicotine and their controls were kept in constant darkness, as nicotine is light-sensitive.

Generation of LRRK2^{G2019S} hIPSCs

Usage of hIPSCs, including KOLF2-1J, was ethically approved (EC reference S65730). HiPSC from the KOLF2-1J [45] were used as control. KOLF2-1J was a gift by William C. Skarnes from The Jackson Laboratories. LRRK2 p.G2019S was engineered in the KOLF2-1J iPSC line, by means of CRISPR/Cas9 gene editing following [84]. Briefly, KOLF2-1J iPSCs were nucleofected with Lonza Nucleofector IV using Cas9 HiFi protein (IDT), a synthetic guide RNA (Synthego) and a single strand oligodeoxynucleotide (ssODN; IDT) as a donor template. Four days post-transfection, cells were dissociated to single cells and seeded at low density in 10cm plates. Single colonies were isolated in 96-well plate and sampled for molecular analysis by PCR followed by Sanger sequencing. More than 90% of the colonies harbored the LRRK2 p.G2019S mutation in homozygosis. Selected clones were karyotyped by means of comparative genomic hybridization (CGH) and stained for pluripotency markers.

To build the transfer vector pLenti-hSynI-mRuby2-T2A-GCaMP6f-Wpre, the hSynI-mRuby2-T2A-GCaMP6f-Wpre fragment was PCR amplified from pAAV-hSyn1-mRuby2-GSG-P2A-GCaMP6f-WPRE-pA, which was a gift from Tobias Bonhoeffer & Mark Huebener & Tobias Rose (Addgene plasmid #50943) and was introduced into a regular 3rd generation lentiviral backbone.

iPSC differentiation to ventral midbrain dopamine neurons

On day -1, 400.000 hiPSC/cm2 were seeded on Matrigel coated 6-well plate wells in StemFlex medium supplemented with 10 µM Rho kinase inhibitor (RI). On day 0, medium was switched to a 1:1 mix of DMEM/F-12 and Neurobasal supplemented with 0.5x N2, 0.5x B27 without vitamin A, GlutaMAX, Penstrep, non-essential amino acids and 10 µM β-mercaptoethanol (all from Life Technologies), insulin (5 µg/ml, Sigma) supplemented with LDN193189 (500 nM, Sigma), SB431542 (10 µM, Tocris), SHH-C24II (200 ng/ml, Miltenyi Biotec), Purmorphamine (1 µM, Miltenyi-Biotec). CHIR99021 was added to the medium from day 3 to day 13 (CHIR; 1.5 µM, Stemcell Technologies). SB431542, SHH-C24II and Purmorphamine were withdrawn from the medium at day 9. FGF8b (100 ng/mL, Miltenyi-Biotec) was added to the medium from day 9 until day 16. Cells were split 1:1 at day 11 and medium was switched to Neurobasal supplemented with 0.5x N2, 0.5x B27 without vitamin A, Penstrep, GlutaMAX. At day 16, cells were split 1:2 and the medium was switched to terminal differentiation medium consisting of Neurobasal-A supplemented with 1xB27 supplement without vitamin A, GlutaMAX, Penstrep containing BDNF (brain-derived neurotrophic factor, 10 ng/ml; Miltenyi-Biotec), ascorbic acid (0.2 mM, Sigma), GDNF (glial cell line-derived neurotrophic factor, 10 ng/ml; Miltenyi-Biotec), dibutyryl cAMP (0.2 mM; Sigma), SR11237 (100 nM, Tocris), and DAPT (10 µM; Tocris). On day 20, ventral midbrain neural progenitors were cryopreserved and quality controlled. To obtain mature neurons, neural progenitor cells were terminally differentiated on coverslips previously coated with poly-D-lysine (50 µg/mL)/mouse laminin (1 µg/mL) in terminal differentiation medium for additional 40 days.

Immunostaining of iPSC and the differentiation products

For the characterization of iPSCs, ventral midbrain floor plate progenitors, cells were fixed for 15 min in 4 % formaldehyde at the pluripotency stage, day 20 of differentiation or day 60 of differentiation, respectively. Cells were blocked for 1 h at room temperature with 3 % normal goat serum + 0.3 % Triton X-100 (Sigma) in DPBS supplemented with Ca2+ and Mg2+ (Life Technologies). Primary antibodies were incubated overnight at 4°C in blocking solution. Secondary antibodies were incubated for 1 h at room temperature in blocking solution. Coverslips were mounted in Mowiol (Sigma) and imaged on an upright Nikon A1R confocal microscope equipped with a DIC N2 20X lens (NA 0.75). Z-stacks were acquired with pinhole of 1 Airy unit, a Galvano scanner with line averaging of 2, image size of 1024 x 1024 pixels and step intervals of 2 µm.
The following antibodies were used: mouse IgG1 anti-SOX2 [1:200 (Santa Cruz)], rabbit anti-OCT4 [1:50 (Abcam)], mouse IgG1 anti-NANOG [1:50 (Santa Cruz)], mouse IgM anti-TRA-1-81 [1:100 (Abcam)], rabbit anti-LMX1A/B [1:1000 (Millipore)], mouse IgG2a anti-FOXA2 [1:250 (Santa Cruz)], mouse IgG1 anti-Engrailed-1 [1:100 (DSHB, 4G11)], mouse IgG2a anti-OTX2 [1:100 (Santa Cruz)], rabbit anti-TH [1:500 (Sigma)], mouse IgG1 anti-MAP2 [1:1000

(Sigma)], Alexa Fluor-488/ Alexa Fluor-555/ Alexa Fluor-647 conjugated secondary antibodies [1:500 (Invitrogen)].

iPSC imaging and drug treatment

Day 40 dopamine neurons were treated for the following 19 days with 1 µM nicotine or with 1 µM nicotine plus 1 µM of the nicotinic receptor antagonist Mecamylamine hydrochloride (both from Sigma). Day 50 dopamine neurons were transduced with a lentiviral vector expressing mRuby2-T2A-GCaMP6f. Transduction efficacy was assessed by directly visualizing mRuby2 red fluorescence. Drug treatment was interrupted 1 day before analysis. For calcium imaging, cell culture medium was switched to BrainPhys Imaging medium (Stem Cell Technologies) supplemented with B27 plus (Life Technologies), PenStrep (Life Technologies), GDNF (10 ng/mL), BDNF (10 ng/mL), (0.2 mM, Sigma), dibutyryl cAMP (0.2 mM; Sigma) and SR11237 (100 nM, Tocris).
Cells were imaged at 37°C at a wide field fluorescence microscope (Nikon) equipped with a Hamamatsu camera and a 20×/NA=0.9 water-immersion objective. For each plate, at least 2 areas were imaged for six minutes at a framerate of 5Hz. Images were analyzed using Fiji [64] [64]. All visible cell bodies in the field of view defined a region of interest (ROI), background fluorescence was subtracted to correct for bleaching. Basal fluorescence F_0 in each ROI was determined by the minimal average of five frames and the change of fluorescence over time was calculated by $F-F_0/F_0$. Values above 2xStdDev of the baseline frames were considered as activity. Activity is expressed as active frames/total measured frames. The maximal amplitude was counted as amplitude for each neuron.

Quantification and statistical analysis

GraphPad Prism was used for visualization and statistical analysis of results from all but the sequencing experiments. Males and females were quantified separately, and results pooled later because they did not show significant differences. Datasets were checked for normal distribution and then analyzed with ANOVA and subsequent multiple pairwise comparisons using Dunnett's test when comparing to a general control, or Bonferroni-correction of p-values when comparing different control-test pairs.

Key resources table

REAGENT RESOURCE	SOURCE	IDENTIFIER
Antibodies		
mouse anti-DLG (1:100)	DSHB, Iowa, US	4F3
rabbit anti-TH (1:200)	Sigma Aldrich	AB152
chicken anti-GFP (1:500)	aves labs inc	GFP-1020
Alexa 488 goat anti-chicken (1:500)	Invitrogen, CA, US	A11039
Alexa 488 goat anti-rabbit (1:500)	Invitrogen, CA, US	A11034
Alexa 555 goat anti-mouse (1:500)	Invitrogen, CA, US	A21424
Bacterial and Virus Strains		
Oneshot top10 cells	ThermoFisher Scientific	C404010

Chemicals, Peptides, and Recombinant Proteins		
Ringer's solution	Estes et al., 1996	
TMRE	Abcam, Cambridge, UK	ab113852
Dispase	Sigma Aldrich	D4818
Collagenase	Invitrogen, CA, US	17100-017
Trypsin-EDTA	Invitrogen, CA, US	25300054
Nicotine	Sigma Aldrich	N3876
Critical Commercial Assays		
NEBuilder® HiFi DNA Assembly	New England Biolabs, Inc (NEB)	NEB #E2621
Maxwell RSC instrument and kit	Promega	AS8500, AS1340
Chromium Single Cell 3′ Library & Gel Bead Kit v2	10x Genomics	PN-120237
Chromium Single Cell A Chip Kit	10x Genomics	PN-1000009
Chromium i7 Multiplex Kit	10x Genomics	PN-120262
Chromium Next GEM Single Cell 3' Kit v3	10x Genomics	PN-1000075
Chromium Next GEM Chip B Single Cell Kit	10x Genomics	PN-1000073
Single Index Kit T Set A	10x Genomics	PN-1000213
Experimental Models: Fly Strains		
GH146-Gal4	Stocker et al., 1996	BDSC_30026; FlyBase: FBti0016783
GMR31F10-Gal4 (T1-Gal4)	Jenett et al., 2012	BDSC_49685; FlyBase:
GMR58E02-Gal4 (PAM-Gal4)	Jenett et al., 2012	BDSC_41347;FlyBase: FBti0137105
UAS-GCaMP3	Tian et al., 2009	BDSC_32236; BDSC_32116
UAS-hLRRK2	Venderova et al., 2009	
UAS-hPINK1	Yang et al., 2006	
UAS-YFP-Rab39	Zhang et al., 2007	BDSC_9825; FlyBase: FBti0100878
UAS-Synj	Vanhauwaert et al., 2017	
UAS-mCherry-Atg8a	Chang & Neufeld, 2009	
UAS-GFP-Lamp1	Pulipparacharuvil et al, 2005	
UAS-Hsc70-4	Elefant and Palter, 1999	BDSC_5846; FlyBase: FBti0016220
UAS-fz2-RNAi	Perkins et al., 2015	BDSC_31390; BDSC_67863
UAS-syt7-RNAi	Perkins et al., 2015	BDSC_27279; FlyBase:
UAS-cow-RNAi	Perkins et al., 2015	BDSC_44530; FlyBase:
UAS-para-RNAi	Perkins et al., 2015	BDSC_31676; FlyBase:
UAS-DsCam2 - RNAi	Perkins et al., 2015	BDSC_51839; FlyBase:
UAS-liprin γ - RNAi	Perkins et al., 2015	BDSC_28301; FlyBase:
UAS-beat-IC-RNAi	Perkins et al., 2015	BDSC_64528; FlyBase:
UAS-SOD2		BDSC_24494; FlyBase:
UAS-SOD1		BDSC_24750; BDSC_33605
UAS-tau-RNAi	Perkins et al., 2015	BDSC_28891; BDSC_40875

UAS-GFP-Act5C	Roper et al., 2005	BDSC_9257; BDSC_9258
UAS-mt:lrRNA-RNAi	Perkins et al., 2015	BDSC_41584; FlyBase: FBti0149240
UAS-mt:ND5-RNAi	Perkins et al., 2015	BDSC_77336; FlyBase: FBti0196088
UAS-Lis		BDSC_9914; FlyBase: FBti0076784
UAS-Brp-RNAi	Perkins et al., 2015	BDSC_80449; BDSC_25891
UAS-Aux	this study	
UAS-endoA^{S75D}	this study	
CG5010$^{k.o.}$ (*chchd2*$^{k.o.}$)	this study	
hCHCHD2	this study	
hCHCHD2^{R145Q}	this study	
hCHCHD2^{T61I}	this study	
LRRK$^{k.o.}$	this study	
hLRRK2	this study	
hLRRK2^{G2019S}	this study	
hLRRK2^{Y1699C}	this study	
PINK1$^{k.o.}$	this study	
hPINK1^{P399L}	this study	
hPINK1^{L347P}	this study	
Rab39$^{k.o.}$	this study	
hRab39B	this study	
hRab39B^{G192R}	this study	
hRab39B^{T168K}	this study	
Aux$^{k.o.}$	this study	
hDNAJC6	this study	
Aux^{wt}	this study	
Aux^{R927G}	this study	
Synj$^{k.o.}$	this study	
hSynj1	this study	
Synj^{wt}	this study	
Synj^{R258Q}	this study	
Plasmids		
pCFD4: U6:1-gRNA U6:3-gRNA	Port et al., 2014	RRID:Addgene_49411
pUC19	Norrander et al., 1983	RRID:Addgene_50005
pUAST.attB	Bischof et al., 2007	GenBank:EF362409.1
pFL44S{w+}-attB	Khuong et al., 2013	N/A
pWhite-STAR	Choi et al., 2009	N/A
2XMyc-LRRK2-WT	Greggio et al., 2008	RRID:Addgene_25361
pLenti6-DEST PINK1-V5 WT	Beilina et al., 2005	RRID:Addgene_13320
Software and Algorithms		
Fiji	Schindelin et al., 2012	https://imagej.net/Fiji
Cell Ranger (version 3.0.2)	10xGenomics	https://support.10xgenomics.com/single-cell-gene-expression/software/downloads/latest
Seurat	Satija et al., 2015	
GOrilla	Eden et al., 2009	http://cbl-gorilla.cs.technion.ac.il/

GraphPad Prism	GraphPad software, CA, US	https://www.graphpad.com/scientific-software/prism/
Other and deposited data		
list of oligonucleotides		
list of software used		
SCope Resource Website	Davie et al., 2018 and this study	http://scope.aertslab.org

Supplemental Figures S1 to S6

Figure S1. Related to Figure 1 and 2. Validation of PD knock-ins and annotated t-SNE of single cell RNA-seq data.

(A) RNA expression levels, measured using RT-PCR with primers to the indicated CDS (above the graphs) in heads of the control, and animals with wildtype or pathogenic mutant CDS knock-ins. Data are expressed as percent of control (i.e., endogenous *Drosophila* gene expression). Grey bars indicate variance in control. **(B)** Exemplary survival curves of flies kept under wet starvation, (first row in Figure 1B). **(C)** Exemplary images of TMRE fluorescence at larval NMJs (second row in Figure 1B). TMRE staining correlates to mitochondrial membrane potential. Insets show magnified synaptic boutons. Scale bar: 10 µm. **(D)** Exemplary electroretinogram (ERG) traces in response to 1s light stimulus (third row in Figure 1B). Animals were kept for 7 days in constant light prior to the experiment. Red line is the average of the individual raw data traces that are shown.

(E) Single-cell-RNA-sequencing identifies 186 cell types in the fly brain. T-Sne of 226k cells characterized by single cell sequencing of entire fly brains as shown in Figure 2A. Identified cell types are labeled.

Figure S2. Related to Figure 2. Validation and analysis of single-cell-RNA-sequencing data.

(A) Frequency of individual cell types (olfactory projection neurons, dopaminergic neurons, visual projection neurons) and the sex ratios of the sequenced cells detected across the PD knock-in models and controls. Note we only sequenced males from hPINK1^{P399L} mutants.

(B) Alignment of published transcriptomic profiles defined by bulk sequencing of FAC sorted cell types (y-axis, see also [28]) and the cell types identified in this study (x-axis), validating the identification of cell types in the t-SNE clusters. Green indicates central brain cell types; Blue is optic lobe; Yellow is glia; Grey is others.

(C) Expression level of knocked-in CDS across the cell types, indicating the knocked-in genes are broadly expressed. DAN – dopaminergic neurons (PAM cluster), OPN –olfactory projection neurons, T1 – T1 visual interneurons.

(D) Comparison of two different algorithms to detect cell-type specific DEG (see methods) show similar number of DEG and high correlation of signed p-values.

(E) Graphs showing the number of DEG versus the number of cells in a cluster (each dot is a cell type) for each PD fly model and the model of cell-number-dependency of p-values (dotted line – see methods). Confidence intervals are highlighted in red. Cell types with residuals above confidence intervals are considered affected.

Figure S3. Related to Figure 2. Validation of olfactory behavior defects using different odors.

Top: Quantification of olfactory performance when presenting blends of beer and wine to control (grey), young PD models (clear bars) or wildtype CDS knock-in flies (checkered). n≥5 assays (≥250 flies) per genotype.

Bottom: Olfactory performance of young pathogenic mutant knock-in (and $LRRK^{KO}$) animals combined with a UAS-CDS construct encoding the respective wild type human or fly gene either not expressed (top, clear bars, "UAS-gene") or expressed specifically in OPN using GH146-Gal4 (bottom, checkered bars, "OPN>UAS-gene"). This indicates that expression of wild type CDS in OPN of the familial PD models (and $LRRK^{KO}$) is sufficient to rescue the olfactory performance defect. n≥5 assays (≥250 flies) per genotype. *, $p<0.05$ in ANOVA followed by Dunnett's test. Grey zone indicates the variance of controls.

Figure S4. Related to Figure 3. Single-cell-RNA sequencing of cholinergic regions in post mortem human brain samples.

(A) T-sne of cells characterized in three cholinergic brain regions of ten brains, annotated are either the major cell types (left) or 36 individual identified cell types (numbered, right). N - neurons, OG - oligodendrocytes, ENT -endothelia, EPY - ependymal cells, LM - lymphocyte, MG - microglia, AST - astrocytes, OPC - oligoprecurser cells, U - unknown.

(B) Frequency of the 36 cell types in pooled PD vs. non-PD samples, in individual brain samples, and in the three brain regions.

(C) Frequency of cells expressing cholinergic marker genes *ACHE* and *CHAT*. NBM - Nucleus basalis Meynert, Nac - Nucleus accumbens, Put - Putamen.

Figure S5. Related to Figure 5. Upregulation of protein homeostasis rescues hyposmia across familial models of PD.

Results of a behavioral screen for cell-specific rescue of olfactory preference defects of young PD fly models using up and downregulation of deregulated genes in affected cell types. Genes implicated in the indicated pathways are over expressed or knocked down selectively in OPNs using GH146-Gal4 (OPN>) and UAS-constructs (over expression or RNAi) . UAS-only (-) and OPN>UAS (+) were scored in parallel and are compared to each other. n.d. not determined; Bars represent mean ± s.e.m.; grey zone indicates the variance of controls; n≥5 independent

experiments per genotype, with ~50 flies each; red bars: $p<0.05$ in ANOVA and Bonferroni-corrected comparison to UAS-only control.

Figure S6. Related to Figure 8. Generation and validation of human LRRK2^{G2019S} ventral midbrain DAN.

(A) Schematic representation of gene editing strategy to knock-in the G2019S mutation.

(B) Sanger sequencing of a single gene edited clone showing successful homozygous editing of the indicated nucleotide.

(C) KOLF2-1J LRRK2$^{G2019S/G2019S}$ shows normal expression of pluripotency markers OCT4, SOX2, NANOG and TRA-1-81. Nuclei are counterstained with DAPI. Scale bar is 100 µm.

(D) Quantification of the frequency of dopaminergic (TH+ /MAP2+) neurons. Error bars represent mean ± SEM. Data were collected in three independent vmDAn differentiations. **e,** Differentation protocol used.

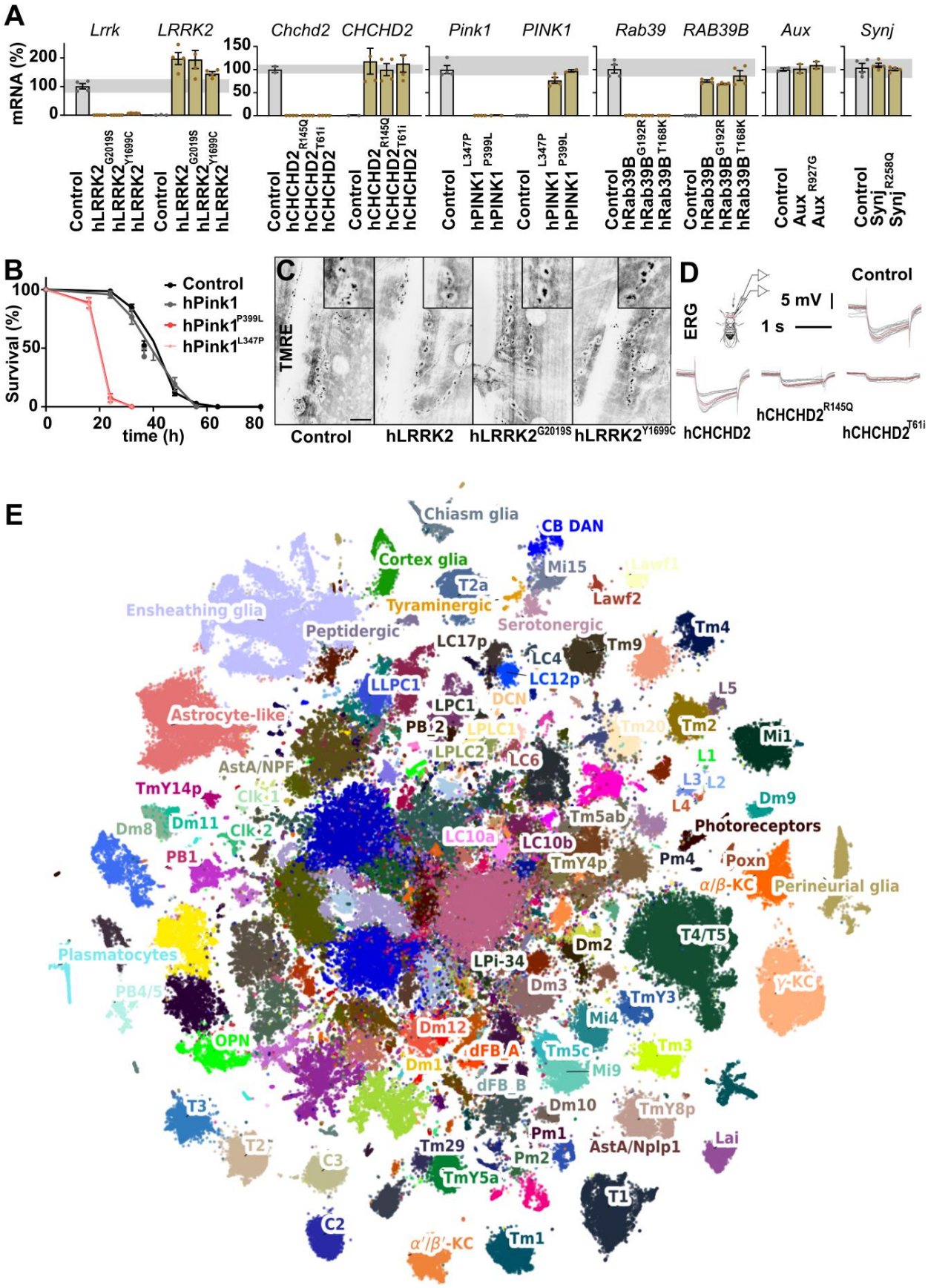
A
Lrrk
LRRK2
Chchd2
CHCHD2
Pink1
PINK1
Rab39
RAB39B
Aux
Synj
mRNA (%)
Control
hLRRK2 G2019S
hLRRK2 Y1699C
hCHCHD2 R145Q
hCHCHD2 T61i
hPINK1 L347P
hPINK1 P399L
hRab39B G192R
hRab39B T168K
Aux R927G
Synj R258Q
B
Survival (%)
time (h)
Control
hPink1
hPink1 P399L
hPink1 L347P
C
TMRE
Control
hLRRK2
hLRRK2 G2019S
hLRRK2 Y1699C
D
ERG
5 mV
1 s
Control
hCHCHD2
hCHCHD2 R145Q
hCHCHD2 T61i
E
Chiasm glia
CB DAN
Cortex glia
Mi15
Lawf1
T2a
Lawf2
Tyraminergic
Ensheathing glia
Serotonergic
Peptidergic
Tm4
LC17p
Tm9
LC4
LC12p
LLPC1
L5
DCN
LPC1
Astrocyte-like
PB2
LPLC1
Tm20
Tm2
Mi1
LPLC2
LC6
L1
AstA/NPF
L3
L2
TmY14p
Clk1
L4
Dm9
Tm5ab
Photoreceptors
Dm8
Dm11
Clk2
LC10a
LC10b
PB1
TmY4p
Pm4
Poxn
α/β-KC
Perineurial glia
T4/T5
Plasmatocytes
Dm2
LPi-34
γ-KC
PB4/5
Dm3
TmY3
Mi4
Dm12
OPN
dFB_A
Tm5c
Tm3
Dm1
Mi9
dFB_B
T3
Dm10
TmY8p
Pm1
Lai
T2
Tm29
AstA/Nplp1
C3
Pm2
TmY5a
T1
C2
α′/β′-KC
Tm1

Figure S1. Related to Figure 1 and 2. Validation of PD knock-ins and annotated t-SNE of single cell RNA-seq data.

(A) RNA expression levels, measured using RT-PCR with primers to the indicated CDS (above the graphs) in heads of the control, and animals with wildtype or pathogenic mutant CDS knock-ins. Data are expressed as percent of control (i.e., endogenous *Drosophila* gene expression). Grey bars indicate variance in control. **(B)** Exemplary survival curves of flies kept under wet starvation, (first row in Figure 1B). **(C)** Exemplary images of TMRE fluorescence at larval NMJs (second row in Figure 1B). TMRE staining correlates to mitochondrial membrane potential. Insets show magnified synaptic boutons. Scale bar: 10 µm. **(D)** Exemplary electroretinogram (ERG) traces in response to 1s light stimulus (third row in Figure 1B). Animals were kept for 7 days in constant light prior to the experiment. Red line is the average of the individual raw data traces that are shown.

(E) Single-cell-RNA-sequencing identifies 186 cell types in the fly brain. T-Sne of 226k cells characterized by single cell sequencing of entire fly brains as shown in Figure 2A. Identified cell types are labeled.

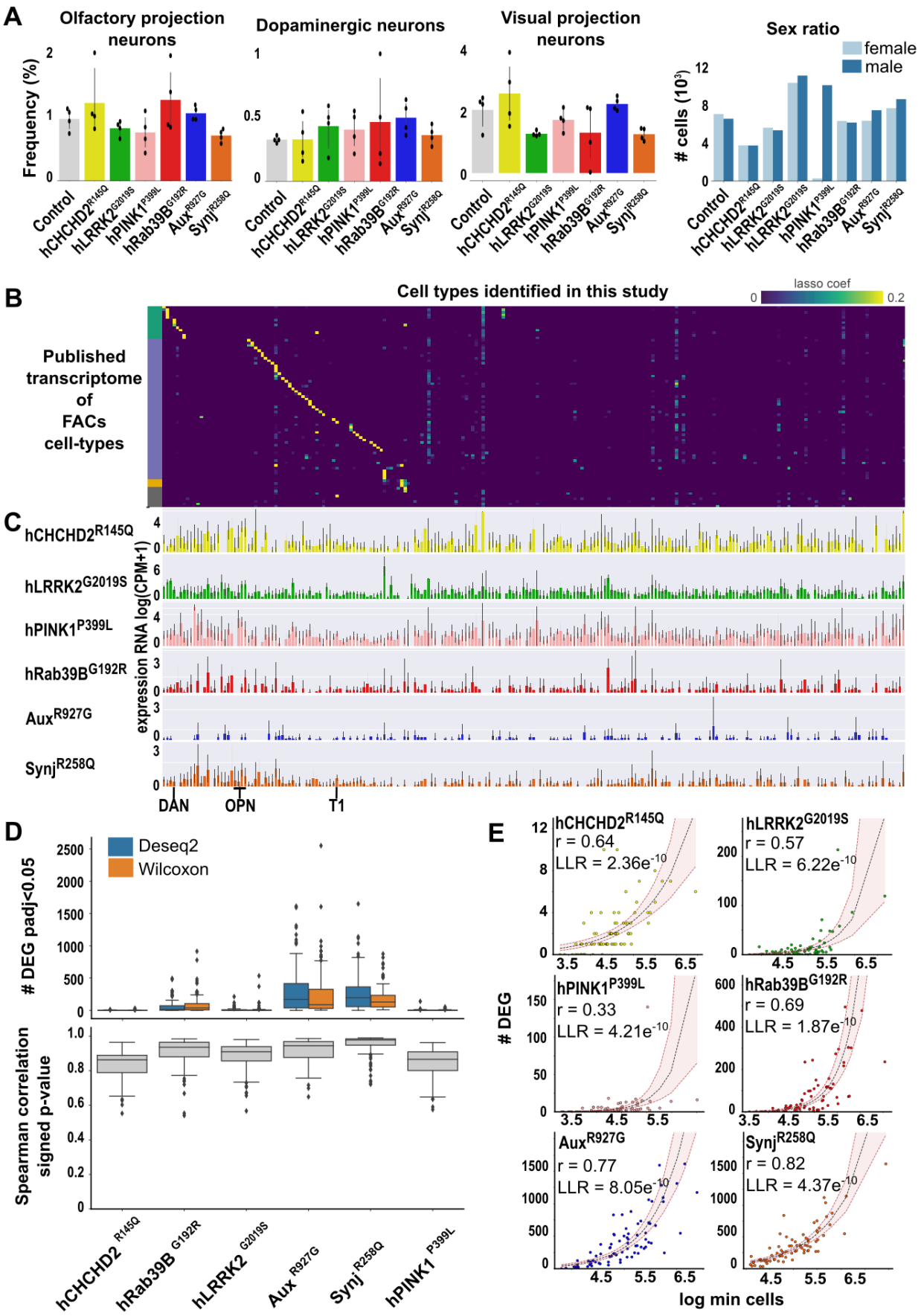
A
Olfactory projection neurons
Dopaminergic neurons
Visual projection neurons
Sex ratio
female
male
Frequency (%)
cells (10³)
Control
hCHCHD2R145Q
hLRRK2G2019S
hPINK1P399L
hRab39BG192R
AuxR927G
SynjR258Q
B
Cell types identified in this study
lasso coef
Published transcriptome of FACs cell-types
C
expression RNA log(CPM+1)
DAN
OPN
T1
D
Deseq2
Wilcoxon
DEG padj<0.05
Spearman correlation signed p-value
E
r = 0.64
LLR = 2.36e-10
r = 0.57
LLR = 6.22e-10
r = 0.33
LLR = 4.21e-10
r = 0.69
LLR = 1.87e-10
r = 0.77
LLR = 8.05e-10
r = 0.82
LLR = 4.37e-10
# DEG
log min cells

Figure S2. Related to Figure 2. Validation and analysis of single-cell-RNA-sequencing data.

(A) Frequency of individual cell types (olfactory projection neurons, dopaminergic neurons, visual projection neurons) and the sex ratios of the sequenced cells detected across the PD knock-in models and controls. Note we only sequenced males from hPINK1^{P399L} mutants.

(B) Alignment of published transcriptomic profiles defined by bulk sequencing of FAC sorted cell types (y-axis, see also [28]) and the cell types identified in this study (x-axis), validating the identification of cell types in the t-SNE clusters. Green indicates central brain cell types; Blue is optic lobe; Yellow is glia; Grey is others.

(C) Expression level of knocked-in CDS across the cell types, indicating the knocked-in genes are broadly expressed. DAN – dopaminergic neurons (PAM cluster), OPN –olfactory projection neurons, T1 – T1 visual interneurons.

(D) Comparison of two different algorithms to detect cell-type specific DEG (see methods) show similar number of DEG and high correlation of signed p-values.

(E) Graphs showing the number of DEG versus the number of cells in a cluster (each dot is a cell type) for each PD fly model and the model of cell-number-dependency of p-values (dotted line – see methods). Confidence intervals are highlighted in red. Cell types with residuals above confidence intervals are considered affected.

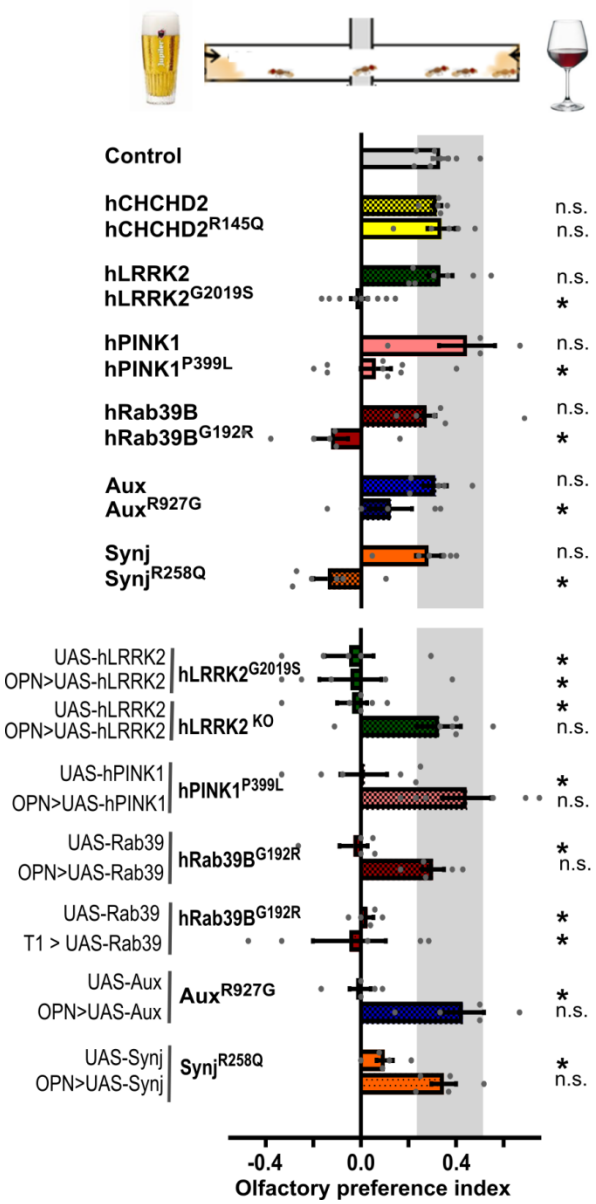

Figure S3. Related to Figure 2. Validation of olfactory behavior defects using different odors.

Top: Quantification of olfactory performance when presenting blends of beer and wine to control (grey), young PD models (clear bars) or wildtype CDS knock-in flies (checkered). n≥5 assays (≥250 flies) per genotype.

Bottom: Olfactory performance of young pathogenic mutant knock-in (and $LRRK^{KO}$) animals combined with a UAS-CDS construct encoding the respective wild type human or fly gene either not expressed (top, clear bars, "UAS-gene") or expressed specifically in OPN using GH146-Gal4 (bottom, checkered bars, "OPN>UAS-gene"). This indicates that expression of wild type CDS in OPN of the familial PD models (and $LRRK^{KO}$) is sufficient to rescue the olfactory performance defect. n≥5 assays (≥250 flies) per genotype. *, $p<0.05$ in ANOVA followed by Dunnett's test. Grey zone indicates the variance of controls.

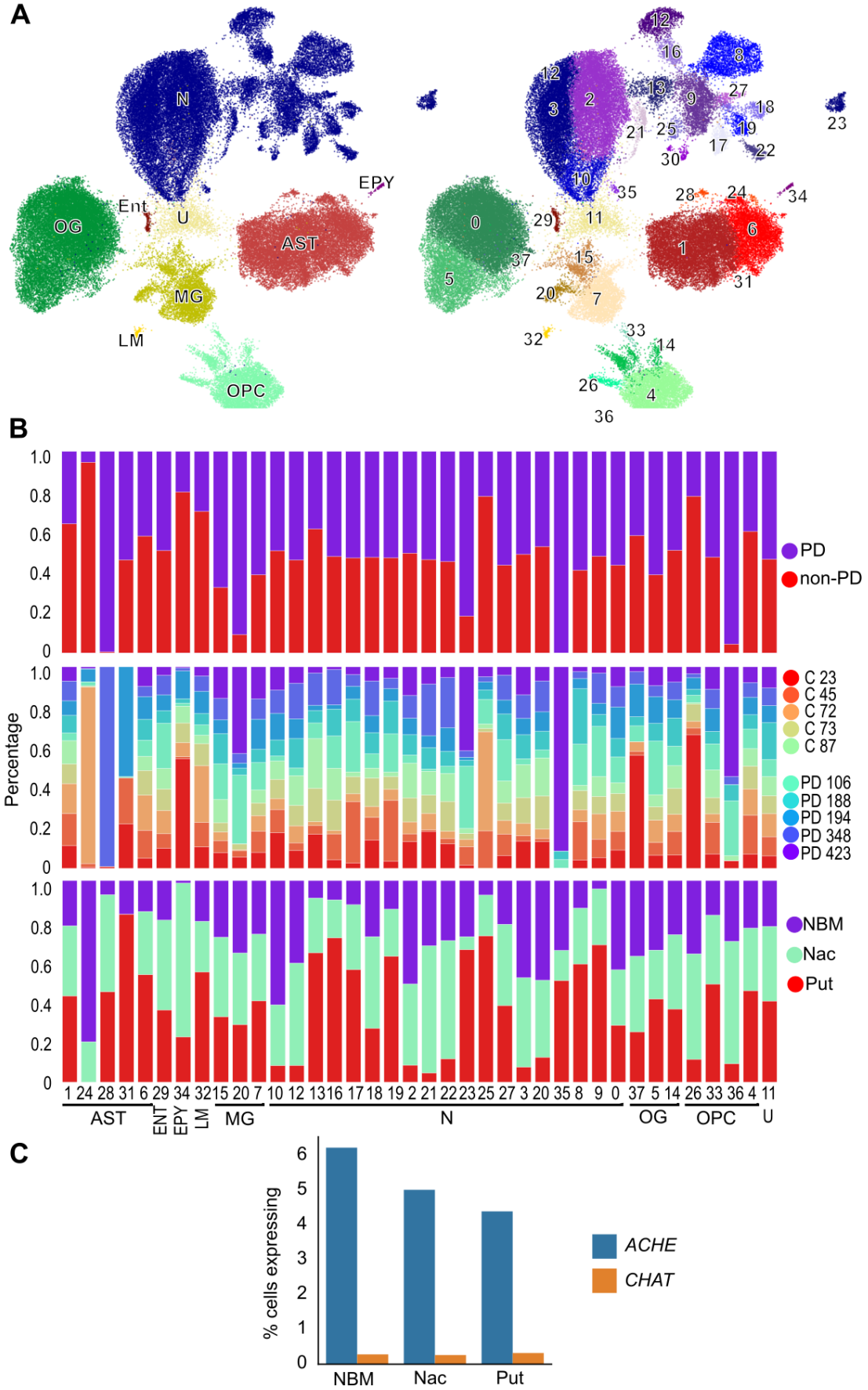
A
N
OG
Ent
U
AST
EPY
MG
LM
OPC
B
Percentage
PD
non-PD
C 23
C 45
C 72
C 73
C 87
PD 106
PD 188
PD 194
PD 348
PD 423
NBM
Nac
Put
AST
ENT
EPY
LM
MG
N
OG
OPC
U
C
% cells expressing
ACHE
CHAT
NBM
Nac
Put

Figure S4. Related to Figure 3. Single-cell-RNA sequencing of cholinergic regions in post mortem human brain samples.

(A) T-sne of cells characterized in three cholinergic brain regions of ten brains, annotated are either the major cell types (left) or 36 individual identified cell types (numbered, right). N - neurons, OG - oligodendrocytes, ENT -endothelia, EPY - ependymal cells, LM - lymphocyte, MG - microglia, AST - astrocytes, OPC - oligoprecurser cells, U - unknown.

(B) Frequency of the 36 cell types in pooled PD vs. non-PD samples, in individual brain samples, and in the three brain regions.

(C) Frequency of cells expressing cholinergic marker genes *ACHE* and *CHAT*. NBM - Nucleus basalis Meynert, Nac - Nucleus accumbens, Put - Putamen.

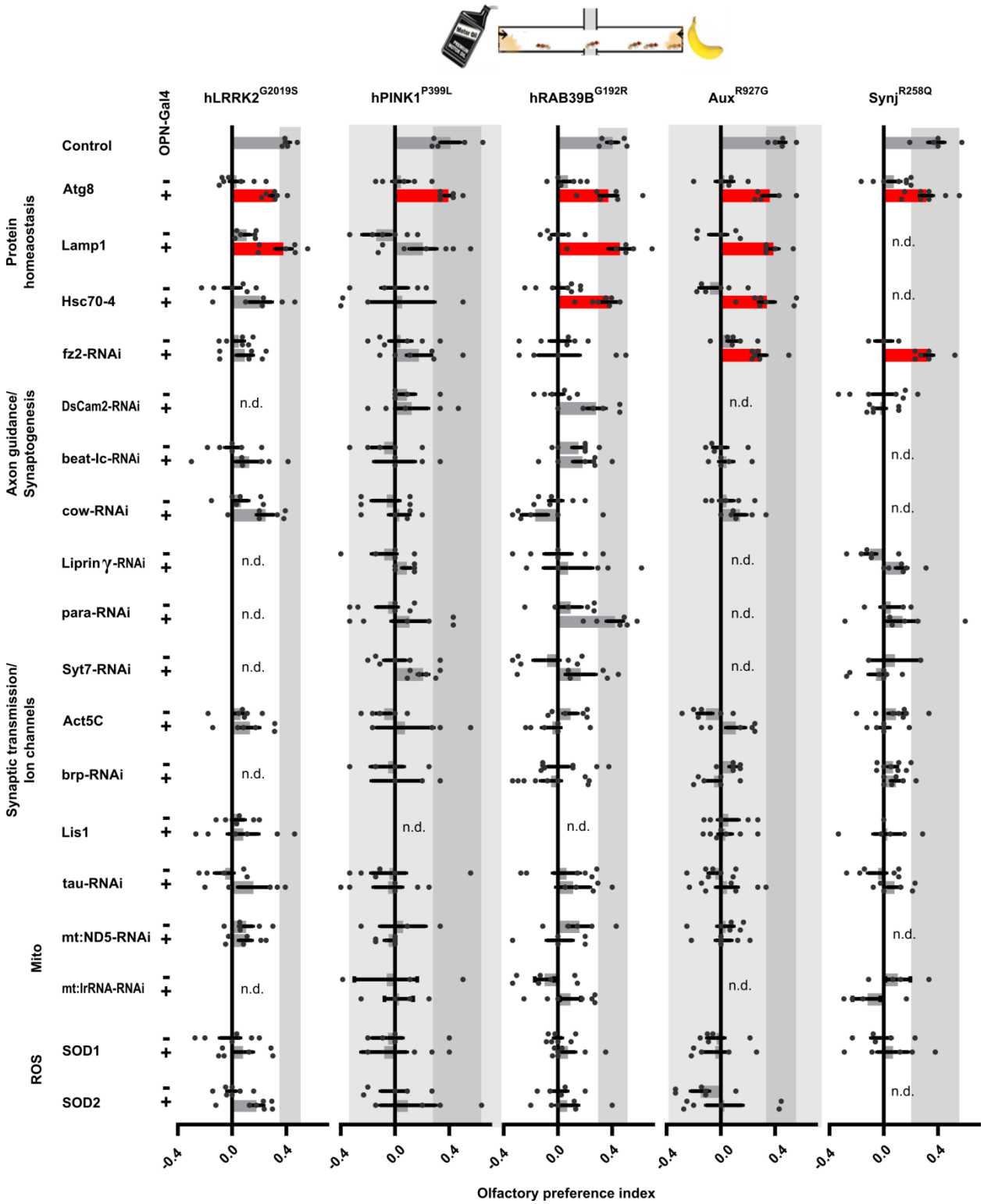

Figure S5. Related to Figure 5. Upregulation of protein homeostasis rescues hyposmia across familial models of PD.

Results of a behavioral screen for cell-specific rescue of olfactory preference defects of young PD fly models using up and downregulation of deregulated genes in affected cell types. Genes implicated in the indicated pathways are over expressed or knocked down selectively in OPNs

using GH146-Gal4 (OPN>) and UAS-constructs (over expression or RNAi) . UAS-only (-) and OPN>UAS (+) were scored in parallel and are compared to each other. n.d. not determined; Bars represent mean ± s.e.m.; grey zone indicates the variance of controls; $n \geq 5$ independent experiments per genotype, with ~50 flies each; red bars: $p<0.05$ in ANOVA and Bonferroni-corrected comparison to UAS-only control.

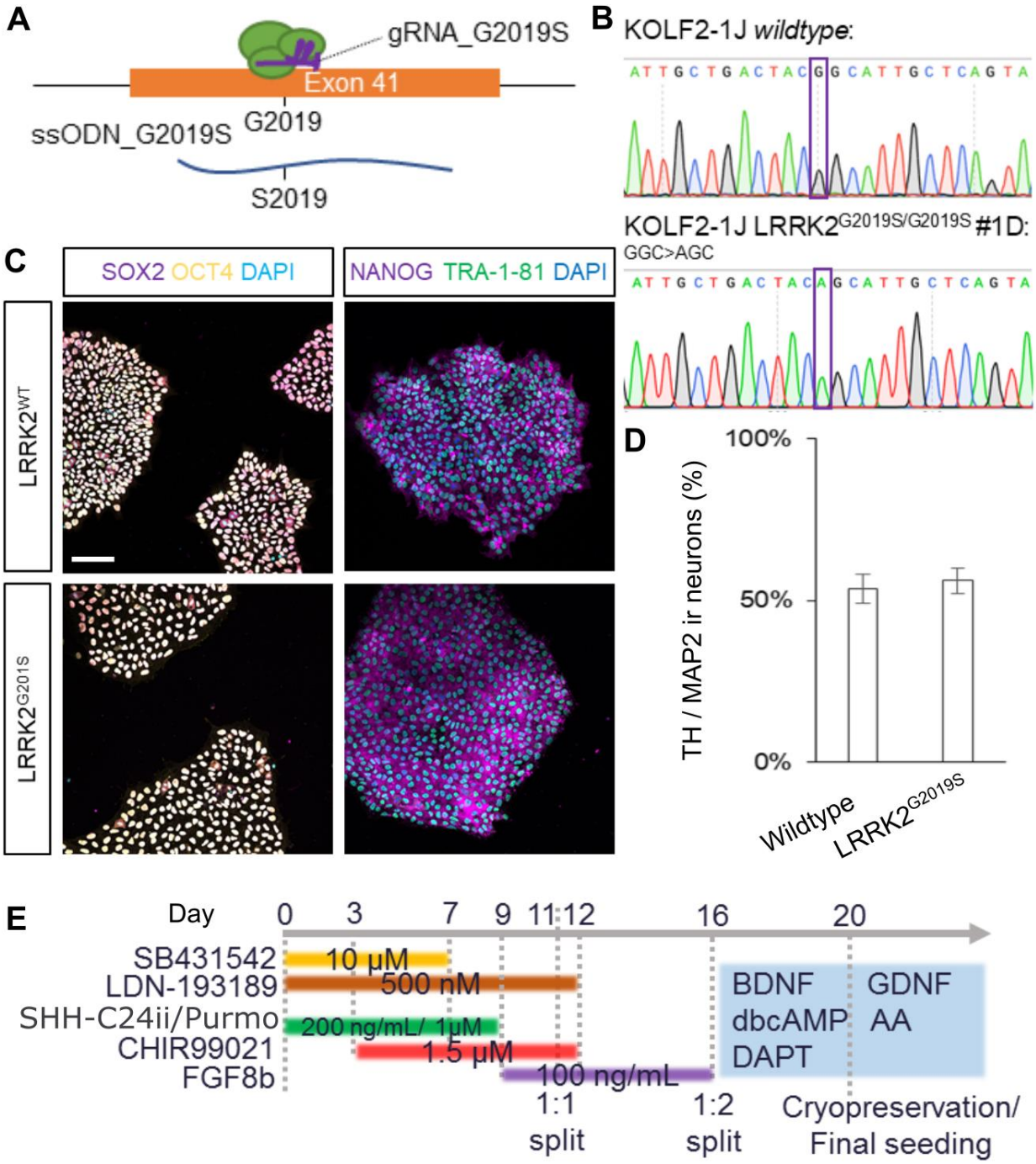

Figure S6. Related to Figure 8. Generation and validation of human LRRK2^{G2019S} ventral midbrain DAN.

(A) Schematic representation of gene editing strategy to knock-in the G2019S mutation.

(B) Sanger sequencing of a single gene edited clone showing successful homozygous editing of the indicated nucleotide.

(C) KOLF2-1J LRRK2$^{G2019S/G2019S}$ shows normal expression of pluripotency markers OCT4, SOX2, NANOG and TRA-1-81. Nuclei are counterstained with DAPI. Scale bar is 100 µm.

(D) Quantification of the frequency of dopaminergic (TH+ /MAP2+) neurons. Error bars represent mean ± SEM. Data were collected in three independent vmDAn differentiations. **e,** Differentation protocol used.

References

1. Parkinson J. 2002. An essay on the shaking palsy. 1817. J Neuropsychiatry Clin Neurosci. 14(2):223-236; discussion 222.
2. Ansari KA, Johnson A. 1975. Olfactory function in patients with parkinson's disease. J Chronic Dis. 28(9):493-497.
3. Doty RL, Deems DA, Stellar S. 1988. Olfactory dysfunction in parkinsonism: A general deficit unrelated to neurologic signs, disease stage, or disease duration. Neurology. 38(8):1237-1244.
4. Schapira AHV, Chaudhuri KR, Jenner P. 2017. Non-motor features of parkinson disease. Nat Rev Neurosci. 18(8):509.
5. Chase BA, Markopoulou K. 2020. Olfactory dysfunction in familial and sporadic parkinson's disease. Front Neurol. 11:447.
6. Kalia LV, Lang AE. 2015. Parkinson's disease. Lancet. 386(9996):896-912.
7. Haehner A, Boesveldt S, Berendse HW, Mackay-Sim A, Fleischmann J, Silburn PA, Johnston AN, Mellick GD, Herting B, Reichmann H et al. 2009. Prevalence of smell loss in parkinson's disease--a multicenter study. Parkinsonism Relat Disord. 15(7):490-494.
8. Doty RL. 2012. Olfactory dysfunction in parkinson disease. Nat Rev Neurol. 8(6):329-339.
9. Double KL, Rowe DB, Hayes M, Chan DK, Blackie J, Corbett A, Joffe R, Fung VS, Morris J, Halliday GM. 2003. Identifying the pattern of olfactory deficits in parkinson disease using the brief smell identification test. Arch Neurol. 60(4):545-549.
10. Mueller A, Abolmaali ND, Hakimi AR, Gloeckler T, Herting B, Reichmann H, Hummel T. 2005. Olfactory bulb volumes in patients with idiopathic parkinson's disease a pilot study. J Neural Transm (Vienna). 112(10):1363-1370.
11. Witt M, Bormann K, Gudziol V, Pehlke K, Barth K, Minovi A, Hähner A, Reichmann H, Hummel T. 2009. Biopsies of olfactory epithelium in patients with parkinson's disease. Mov Disord. 24(6):906-914.
12. Harvey JD, Heinbockel T. 2018. Neuromodulation of synaptic transmission in the main olfactory bulb. Int J Environ Res Public Health. 15(10).
13. Huisman E, Uylings HB, Hoogland PV. 2004. A 100% increase of dopaminergic cells in the olfactory bulb may explain hyposmia in parkinson's disease. Mov Disord. 19(6):687-692.
14. Zhang S, Xiao Q, Le W. 2015. Olfactory dysfunction and neurotransmitter disturbance in olfactory bulb of transgenic mice expressing human a53t mutant α-synuclein. PLoS One. 10(3):e0119928.
15. Mundiñano IC, Hernandez M, Dicaudo C, Ordoñez C, Marcilla I, Tuñon MT, Luquin MR. 2013. Reduced cholinergic olfactory centrifugal inputs in patients with neurodegenerative disorders and mptp-treated monkeys. Acta Neuropathol. 126(3):411-425.

16. Taguchi T, Ikuno M, Yamakado H, Takahashi R. 2020. Animal model for prodromal parkinson's disease. Int J Mol Sci. 21(6).
17. Karimi-Moghadam A, Charsouei S, Bell B, Jabalameli MR. 2018. Parkinson disease from mendelian forms to genetic susceptibility: New molecular insights into the neurodegeneration process. Cell Mol Neurobiol. 38(6):1153-1178.
18. Hindle S, Afsari F, Stark M, Middleton CA, Evans GJ, Sweeney ST, Elliott CJ. 2013. Dopaminergic expression of the parkinsonian gene lrrk2-g2019s leads to non-autonomous visual neurodegeneration, accelerated by increased neural demands for energy. Hum Mol Genet. 22(11):2129-2140.
19. Morais VA, Verstreken P, Roethig A, Smet J, Snellinx A, Vanbrabant M, Haddad D, Frezza C, Mandemakers W, Vogt-Weisenhorn D et al. 2009. Parkinson's disease mutations in pink1 result in decreased complex i activity and deficient synaptic function. EMBO Mol Med. 1(2):99-111.
20. Ng CH, Guan MS, Koh C, Ouyang X, Yu F, Tan EK, O'Neill SP, Zhang X, Chung J, Lim KL. 2012. Amp kinase activation mitigates dopaminergic dysfunction and mitochondrial abnormalities in drosophila models of parkinson's disease. J Neurosci. 32(41):14311-14317.
21. Mortiboys H, Johansen KK, Aasly JO, Bandmann O. 2010. Mitochondrial impairment in patients with parkinson disease with the g2019s mutation in lrrk2. Neurology. 75(22):2017-2020.
22. Hoffmann AA, Harshman LG. 1999. Desiccation and starvation resistance in drosophila: Patterns of variation at the species, population and intrapopulation levels. Heredity (Edinb). 83 (Pt 6):637-643.
23. Liu YT, Huang X, Nguyen D, Shammas MK, Wu BP, Dombi E, Springer DA, Poulton J, Sekine S, Narendra DP. 2020. Loss of chchd2 and chchd10 activates oma1 peptidase to disrupt mitochondrial cristae phenocopying patient mutations. Hum Mol Genet. 29(9):1547-1567.
24. Vanhauwaert R, Kuenen S, Masius R, Bademosi A, Manetsberger J, Schoovaerts N, Bounti L, Gontcharenko S, Swerts J, Vilain S et al. 2017. The sac1 domain in synaptojanin is required for autophagosome maturation at presynaptic terminals. EMBO J. 36(10):1392-1411.
25. Song L, He Y, Ou J, Zhao Y, Li R, Cheng J, Lin CH, Ho MS. 2017. Auxilin underlies progressive locomotor deficits and dopaminergic neuron loss in a drosophila model of parkinson's disease. Cell Rep. 18(5):1132-1143.
26. De Rose F, Marotta R, Poddighe S, Talani G, Catelani T, Setzu MD, Solla P, Marrosu F, Sanna E, Kasture S et al. 2016. Functional and morphological correlates in the drosophila lrrk2 loss-of-function model of parkinson's disease: Drug effects of withania somnifera (dunal) administration. PLoS One. 11(1):e0146140.
27. Riemensperger T, Issa AR, Pech U, Coulom H, Nguyễn MV, Cassar M, Jacquet M, Fiala A, Birman S. 2013. A single dopamine pathway underlies progressive locomotor deficits in a drosophila model of parkinson disease. Cell Rep. 5(4):952-960.
28. Davie K, Janssens J, Koldere D, De Waegeneer M, Pech U, Kreft Ł, Aibar S, Makhzami S, Christiaens V, Bravo González-Blas C et al. 2018. A single-cell transcriptome atlas of the aging drosophila brain. Cell. 174(4):982-998.e920.
29. Janssens J, Aibar S, Taskiran II, Ismail JN, Gomez AE, Aughey G, Spanier KI, De Rop FV, González-Blas CB, Dionne M et al. 2022. Decoding gene regulation in the fly brain. Nature. 601(7894):630-636.

30. Wang T, Li B, Nelson CE, Nabavi S. 2019. Comparative analysis of differential gene expression analysis tools for single-cell rna sequencing data. BMC Bioinformatics. 20(1):40.
31. Masse NY, Turner GC, Jefferis GS. 2009. Olfactory information processing in drosophila. Curr Biol. 19(16):R700-713.
32. West AB, Moore DJ, Biskup S, Bugayenko A, Smith WW, Ross CA, Dawson VL, Dawson TM. 2005. Parkinson's disease-associated mutations in leucine-rich repeat kinase 2 augment kinase activity. Proc Natl Acad Sci U S A. 102(46):16842-16847.
33. Arendt T, Bigl V, Arendt A, Tennstedt A. 1983. Loss of neurons in the nucleus basalis of meynert in alzheimer's disease, paralysis agitans and korsakoff's disease. Acta Neuropathol. 61(2):101-108.
34. Eden E, Navon R, Steinfeld I, Lipson D, Yakhini Z. 2009. Gorilla: A tool for discovery and visualization of enriched go terms in ranked gene lists. BMC Bioinformatics. 10:48.
35. Koopmans F, van Nierop P, Andres-Alonso M, Byrnes A, Cijsouw T, Coba MP, Cornelisse LN, Farrell RJ, Goldschmidt HL, Howrigan DP et al. 2019. Syngo: An evidence-based, expert-curated knowledge base for the synapse. Neuron. 103(2):217-234.e214.
36. Uytterhoeven V, Kuenen S, Kasprowicz J, Miskiewicz K, Verstreken P. 2011. Loss of skywalker reveals synaptic endosomes as sorting stations for synaptic vesicle proteins. Cell. 145(1):117-132.
37. Gorenberg EL, Chandra SS. 2017. The role of co-chaperones in synaptic proteostasis and neurodegenerative disease. Front Neurosci. 11:248.
38. Snead D, Eliezer D. 2019. Intrinsically disordered proteins in synaptic vesicle trafficking and release. J Biol Chem. 294(10):3325-3342.
39. Ringstad N, Nemoto Y, De Camilli P. 1997. The sh3p4/sh3p8/sh3p13 protein family: Binding partners for synaptojanin and dynamin via a grb2-like src homology 3 domain. Proc Natl Acad Sci U S A. 94(16):8569-8574.
40. Verstreken P, Kjaerulff O, Lloyd TE, Atkinson R, Zhou Y, Meinertzhagen IA, Bellen HJ. 2002. Endophilin mutations block clathrin-mediated endocytosis but not neurotransmitter release. Cell. 109(1):101-112.
41. Chang D, Nalls MA, Hallgrímsdóttir IB, Hunkapiller J, van der Brug M, Cai F, Kerchner GA, Ayalon G, Bingol B, Sheng M et al. 2017. A meta-analysis of genome-wide association studies identifies 17 new parkinson's disease risk loci. Nat Genet. 49(10):1511-1516.
42. Nalls MA, Blauwendraat C, Vallerga CL, Heilbron K, Bandres-Ciga S, Chang D, Tan M, Kia DA, Noyce AJ, Xue A et al. 2019. Identification of novel risk loci, causal insights, and heritable risk for parkinson's disease: A meta-analysis of genome-wide association studies. Lancet Neurol. 18(12):1091-1102.
43. Germer EL, Imhoff S, Vilariño-Güell C, Kasten M, Seibler P, Brüggemann N, Klein C, Trinh J, Consortium IPsDG. 2019. The role of rare coding variants in parkinson's disease gwas loci. Front Neurol. 10:1284.
44. Soukup SF, Kuenen S, Vanhauwaert R, Manetsberger J, Hernández-Díaz S, Swerts J, Schoovaerts N, Vilain S, Gounko NV, Vints K et al. 2016. A lrrk2-dependent endophilina phosphoswitch is critical for macroautophagy at presynaptic terminals. Neuron. 92(4):829-844.
45. Pantazis CB, Yang A, Lara E, McDonough JA, Blauwendraat C, Peng L, Oguro H, Kanaujiya J, Zou J, Sebesta D et al. 2022. A reference human induced pluripotent stem cell line for large-scale collaborative studies. Cell Stem Cell. 29(12):1685-1702.e1622.

46. Braak H, Rüb U, Gai WP, Del Tredici K. 2003. Idiopathic parkinson's disease: Possible routes by which vulnerable neuronal types may be subject to neuroinvasion by an unknown pathogen. J Neural Transm (Vienna). 110(5):517-536.
47. Kuhl DE, Minoshima S, Fessler JA, Frey KA, Foster NL, Ficaro EP, Wieland DM, Koeppe RA. 1996. In vivo mapping of cholinergic terminals in normal aging, alzheimer's disease, and parkinson's disease. Ann Neurol. 40(3):399-410.
48. Shimada H, Hirano S, Shinotoh H, Aotsuka A, Sato K, Tanaka N, Ota T, Asahina M, Fukushi K, Kuwabara S et al. 2009. Mapping of brain acetylcholinesterase alterations in lewy body disease by pet. Neurology. 73(4):273-278.
49. Bohnen NI, Müller ML, Kotagal V, Koeppe RA, Kilbourn MA, Albin RL, Frey KA. 2010. Olfactory dysfunction, central cholinergic integrity and cognitive impairment in parkinson's disease. Brain. 133(Pt 6):1747-1754.
50. Baron JA. 1996. Beneficial effects of nicotine and cigarette smoking: The real, the possible and the spurious. Br Med Bull. 52(1):58-73.
51. Hernán MA, Takkouche B, Caamaño-Isorna F, Gestal-Otero JJ. 2002. A meta-analysis of coffee drinking, cigarette smoking, and the risk of parkinson's disease. Ann Neurol. 52(3):276-284.
52. Braak H, Del Tredici K, Rüb U, de Vos RA, Jansen Steur EN, Braak E. 2003. Staging of brain pathology related to sporadic parkinson's disease. Neurobiol Aging. 24(2):197-211.
53. Webb JL, Ravikumar B, Atkins J, Skepper JN, Rubinsztein DC. 2003. Alpha-synuclein is degraded by both autophagy and the proteasome. J Biol Chem. 278(27):25009-25013.
54. Sarkar S, Davies JE, Huang Z, Tunnacliffe A, Rubinsztein DC. 2007. Trehalose, a novel mtor-independent autophagy enhancer, accelerates the clearance of mutant huntingtin and alpha-synuclein. J Biol Chem. 282(8):5641-5652.
55. Chu Y, Dodiya H, Aebischer P, Olanow CW, Kordower JH. 2009. Alterations in lysosomal and proteasomal markers in parkinson's disease: Relationship to alpha-synuclein inclusions. Neurobiol Dis. 35(3):385-398.
56. Friedman LG, Lachenmayer ML, Wang J, He L, Poulose SM, Komatsu M, Holstein GR, Yue Z. 2012. Disrupted autophagy leads to dopaminergic axon and dendrite degeneration and promotes presynaptic accumulation of α-synuclein and lrrk2 in the brain. J Neurosci. 32(22):7585-7593.
57. Wilson RI. 2013. Early olfactory processing in drosophila: Mechanisms and principles. Annu Rev Neurosci. 36:217-241.
58. Wu H, Williams J, Nathans J. 2014. Complete morphologies of basal forebrain cholinergic neurons in the mouse. Elife. 3:e02444.
59. Wilson CJ, Chang HT, Kitai ST. 1990. Firing patterns and synaptic potentials of identified giant aspiny interneurons in the rat neostriatum. J Neurosci. 10(2):508-519.
60. Ashrafi G, Schlehe JS, LaVoie MJ, Schwarz TL. 2014. Mitophagy of damaged mitochondria occurs locally in distal neuronal axons and requires pink1 and parkin. J Cell Biol. 206(5):655-670.
61. Vijayan V, Verstreken P. 2017. Autophagy in the presynaptic compartment in health and disease. J Cell Biol. 216(7):1895-1906.
62. Choi CM, Vilain S, Langen M, Van Kelst S, De Geest N, Yan J, Verstreken P, Hassan BA. 2009. Conditional mutagenesis in drosophila. Science. 324(5923):54.
63. Jacquemyn J, Kuenen S, Swerts J, Pavie B, Vijayan V, Kilic A, Chabot D, Wang Y-C, Schoovaerts N, Verstreken P. Parkinson mutations in dn*ajc6 c*ause lipid defects and neurodegeneration that are rescued by synj1. bioRxiv 2022.04.27.489745.

64. Schindelin J, Arganda-Carreras I, Frise E, Kaynig V, Longair M, Pietzsch T, Preibisch S, Rueden C, Saalfeld S, Schmid B et al. 2012. Fiji: An open-source platform for biological-image analysis. Nat Methods. 9(7):676-682.
65. Slabbaert JR, Kuenen S, Swerts J, Maes I, Uytterhoeven V, Kasprowicz J, Fernandes AC, Blust R, Verstreken P. 2016. Shawn, the drosophila homolog of slc25a39/40, is a mitochondrial carrier that promotes neuronal survival. J Neurosci. 36(6):1914-1929.
66. Benzer S. 1967. Behavioral mutants of drosophila isolated by countercurrent distribution. Proc Natl Acad Sci U S A. 58(3):1112-1119.
67. Inagaki HK, Kamikouchi A, Ito K. 2010. Methods for quantifying simple gravity sensing in drosophila melanogaster. Nat Protoc. 5(1):20-25.
68. Gramates LS, Marygold SJ, Santos GD, Urbano JM, Antonazzo G, Matthews BB, Rey AJ, Tabone CJ, Crosby MA, Emmert DB et al. 2017. Flybase at 25: Looking to the future. Nucleic Acids Res. 45(D1):D663-D671.
69. Flerin C, Chris, Davie K, Hulselmans G, De Waegeneer M. 2021. *Vib-singlecell-nf/vsn-pipelines:*
V0.27.0 (v0.27.0). Zenodo. https://doi.org/10.5281/ZENODO.3703108.
70. Wolock SL, Lopez R, Klein AM. 2019. Scrublet: Computational identification of cell doublets in single-cell transcriptomic data. Cell Syst. 8(4):281-291.e289.
71. Yang S, Corbett SE, Koga Y, Wang Z, Johnson WE, Yajima M, Campbell JD. 2020. Decontamination of ambient rna in single-cell rna-seq with decontx. Genome Biol. 21(1):57.
72. Li H, Janssens J, De Waegeneer M, Kolluru SS, Davie K, Gardeux V, Saelens W, David FPA, Brbić M, Spanier K et al. 2022. Fly cell atlas: A single-nucleus transcriptomic atlas of the adult fruit fly. Science. 375(6584):eabk2432.
73. Jenett A, Rubin GM, Ngo TT, Shepherd D, Murphy C, Dionne H, Pfeiffer BD, Cavallaro A, Hall D, Jeter J et al. 2012. A gal4-driver line resource for drosophila neurobiology. Cell Rep. 2(4):991-1001.
74. Satija R, Farrell JA, Gennert D, Schier AF, Regev A. 2015. Spatial reconstruction of single-cell gene expression data. Nat Biotechnol. 33(5):495-502.
75. Davis FP, Nern A, Picard S, Reiser MB, Rubin GM, Eddy SR, Henry GL. 2020. A genetic, genomic, and computational resource for exploring neural circuit function. Elife. 9.
76. Jones E. 2001. Ann: Scipy 0.10–scientific computing with python. https://mail.python.org/pipermail/python-list/2001-August/106419.html.
77. Hodge RD, Bakken TE, Miller JA, Smith KA, Barkan ER, Graybuck LT, Close JL, Long B, Johansen N, Penn O et al. 2019. Conserved cell types with divergent features in human versus mouse cortex. Nature. 573(7772):61-68.
78. Auton A, Brooks LD, Durbin RM, Garrison EP, Kang HM, Korbel JO, Marchini JL, McCarthy S, McVean GA, Abecasis GR et al. 2015. A global reference for human genetic variation. Nature. 526(7571):68-74.
79. Kang HM, Subramaniam M, Targ S, Nguyen M, Maliskova L, McCarthy E, Wan E, Wong S, Byrnes L, Lanata CM et al. 2018. Multiplexed droplet single-cell rna-sequencing using natural genetic variation. Nat Biotechnol. 36(1):89-94.
80. Love MI, Huber W, Anders S. 2014. Moderated estimation of fold change and dispersion for rna-seq data with deseq2. Genome Biol. 15(12):550.
81. Tully T, Quinn WG. 1985. Classical conditioning and retention in normal and mutant drosophila melanogaster. J Comp Physiol A. 157(2):263-277.

82. Wu X, Li R, Li Q, Bao H, Wu C. 2016. Comparative transcriptome analysis among parental inbred and crosses reveals the role of dominance gene expression in heterosis in drosophila melanogaster. Sci Rep. 6:21124.
83. Deshpande SA, Carvalho GB, Amador A, Phillips AM, Hoxha S, Lizotte KJ, Ja WW. 2014. Quantifying drosophila food intake: Comparative analysis of current methodology. Nat Methods. 11(5):535-540.
84. Skarnes WC, Pellegrino E, McDonough JA. 2019. Improving homology-directed repair efficiency in human stem cells. Methods. 164-165:18-28.